Research & Technology Centre

[redacted]

REPORT NO: 7-186-088/ , Final CLASS: 4

TITLE: Metallographic Examination of
Corrosion Test Samples

DATE: December 1986 AUTHOR: S. Santyr
TECHNICIANS: M. Chambers
L. Laurin
L. Thompson

APPROVED: J.G.H. Reynolds

TITLE: METALLOGRAPHIC EXAMINATION OF CORROSION TEST SAMPLES

FINAL REPORT

BY

S. Santyr (Volume 1)

G. Weatherly (Volume 2)

Work on this project was conducted under the auspices of the Department of Energy, Mines and Resources

This work was supported (in part) by the Federal Panel on Energy R&D (PERD).

DSS FILE NUMBER: 03SQ.23440-6-9110

DSS CONTRACT NUMBER: 23440-6-9110/01-SQ

EMR SCIENTIFIC AUTHORITY: Dr. R. Brigham

82pp

Executive Summary

An extensive metallographic examination has been carried out on specimens previously subjected to corrosion testing. The work was done in an attempt to determine the relationships between corrosion and microstructure and hardness. Three classes of steel were examined: carbon-manganese, alloyed and micro-alloyed steels.

No clearcut relationship between corrosion and microstructure could be established since all specimens having poor corrosion resistance had similar manganese levels, as well as similar microstructures. Thus, it was difficult to separate these effects. However, it is possible that ferrite with both aligned and non-aligned MAC made up of very coarse carbides is more susceptible to corrosion than other HAZ microstructures.

Key Words: HAZ, microstructure, hardness, preferential corrosion

Sommairé Executif

Un examination métallographique a été fait sur les échantillons déja sujet au test de corrosion. Ces travaux ont été entrepris pour essayer de déterminé des correlations entre la corrosion, la microstructure et la dureté. Trois classe d'aciers ont été examiné: C-Mn, alliés et microalliage.

Aucune correlations entre la corrosion et la microstructure pouvait être établi parce que toutes les échantillons qui avaient une résistance à la corrosion pauvre avaient des niveaux de manganese et des microstructures semblables. Alors, c'était difficile d'y séparé ces effets. D'abord, c'est possible que le ferrite avec chacun MAC aligné et non aligné composé de gros carbide est plus susceptible à la corrosion qu'autre microstructures de HAZ.

1.0 INTRODUCTION

A 50/50 cost shared program was sponsored by The Algoma Steel Corporation Ltd. in conjunction with DSS to study the relative corrodibility of the heat affected zone and weld metal in shipbuilding steels as a function of (a) chemical compositions of the parent steels and weld metals, and (b) heat input. This program was entitled "Evaluation of Weld Zone Corrosion in Shipbuilding Steel Plates for Use in the Arctic Environment"[1].

In this program, eleven different steels with varying Mn levels (.54 to 1.45%) and alloying elements (Cu, Ni, Cr, V, Nb), along with four SMAW electrodes and four SAW wire/flux combinations were employed. Each base plate/welding consumable combination was investigated at two heat input levels - 1.2 and 2.5 kJ/mm for SMAW and 2.5 and 4.0 kJ/mm for SAW.

The objectives of the original program were met in that chemistry and heat input effects on relative corrodibility of the heat affected zone and weld metal were evaluated. However, the results of the very limited metallography carried out indicated the possibility of a relationship between rate of corrosion and the heat affected zone microstructure. For this reason, it was felt that a more extensive metallographic examination could bring to light some important information regarding HAZ microstructure/corrosion relationships.

2.0 OBJECTIVES

The objectives set for the present program are listed as follows:

(a) To qualitatively examine the microstructure found in the weld heat affected zone of specimens from two different corrosion tests - tank tests and galvanostatic anodic dissolution tests.

(b) To identify the preferentially attacked micro and/or macrostructures in the regions examined and compare the results for the two different corrosion test specimens.

(c) To qualitatively examine the precipitates and microconstituents in the weld HAZ of certain selected specimens using electron microscopy.

(d) To perform hardness measurements in the coarse grained HAZ and relate it to the extent of HAZ corrosion as indicated by profilometry data from tank test and anodic dissolution test specimens.

3.0 EXPERIMENTAL

3.1 Materials

3.1.1 Steels

Eleven steels were examined in the original program. These steels were predominantly of Canadian origin with the exception of one American (ASTM A710 Gr A, Cl 3), one Japanese (Kawasaki EH36) and one Belgian (Shoralsim 355Z) steel.

These steels represent a wide range of chemical compositions and processing routes (Table 1). Steels A, D and K are C-Mn steels typical of those which have been traditionally used in ship and icebreaker fabrication. The Mn content of this group of steels is less than 1.1%.

Steels C, F, G, H, J and L are all microalloyed with varying amounts of niobium, vanadium or titanium, and represent a more recent generation of steels that possess excellent notch toughness (equal to or better than EH grade requirements in ABS, DnV and Lloyds specifications) at 350 MPa minimum yield strength level. Two of these steels, F and G, were produced under 50/50 cost shared programs between the Federal Government, Algoma Steel Co. and Stelco Inc., respectively. In general, these steels have higher Mn content (1.24 to 1.45%) and contain small amounts of Ni, Cu, or Cr.

Steel E having the lowest Mn content and greatest amount of alloying elements, has been used for naval ships in the U.S. and steel B, containing Cu, Ni and Cr has improved resistance to atmospheric corrosion. Of these eleven steels, six (B,C,E,F,G,K) were chosen to be used in the Tank test.

3.1.2 Consumables

Eight welding consumables, selected on the basis of expected deposit chemistry and toughness, were evaluated in the program. Four of the consumables were submerged arc welding wire/flux combinations and the other four were shielded metal arc welding electrodes. The undiluted weld metal deposit chemistries are shown in Table 2.

The ESAB OK 73.08 SMAW electrode was chosen because it was developed specifically for weld metal corrosion resistance. E8018-W, a North American weathering grade electrode, like the ESAB electrode gives a deposit alloyed with Cu and Ni. E7018-1 was chosen as a typical electrode which is presently used in shipbuilding applications and E8018-C1 was chosen for its high nickel content (2.15%).

Similarly, the L60/761 SAW combination was chosen as a typical C-Mn consumable which is used in shipbuilding applications. Tibor 22/OP121TT was chosen on the basis of its good toughness properties

at high heat inputs which make it a candidate for use in shipbuilding applications. Thyssen S2-Ni 1/UV420TTR and SD2-3Ni/OP121TT also have excellent toughness properties resulting from varying levels of nickel.

3.1.3 Metallography of As-Received Steels and Consumables

Baseplate microstructures of specimens chosen from the Tank test specimens for examination are shown in Figure 1. These typically show ferrite and pearlite phases with ferritic grain size depending on rolling history. An exception to this is A710 (steel E) which is quenched and precipitation hardened, yielding a fine equiaxed ferrite structure with a uniform distribution of carbides.

Weld metal microstructures of the four consumables chosen for complete examination are shown in Figures 2 and 3. The consumables containing Ni generally contain less acicular ferrite and more ferrite with second phase.

3.2 Metallographic Examination

Of the eleven steels in the original program, the six chosen for the Tank test included steels B, C, E, F, G, and K. The samples from the Tank test chosen for metallographic examination are listed in Table 3.

Selected samples from ten of the original eleven steels were chosen for metallographic examination from the Anodic Dissolution Test specimens as shown in Table 4.

Specimens for examination were mounted and polished to a 1 μm diamond finish. These were etched with 2% nital and examined at nominally 10x, 500x and 1000x magnification on a Unitron optical microscope.

3.3 Hardness Measurements

Hardness measurements were made on the polished specimens using Vickers, 10 kg load hardness equipment. The indentations were made specifically in each of the regions of interest, that is, baseplate, subcritical HAZ (i.e. T_{max}<700°C), intercritical HAZ (i.e. 700°C <T_{max}>800°C), supercritical HAZ (i.e. T_{max}>800°C) and as-deposited weld metal. These identations were generally made as close to the corroded surface as possible.

4.0 OBSERVATIONS AND DISCUSSION

4.1 Metallographic Examination

The results of metallographic examination are presented in Figures 4 through 33. All of the high magnification micrographs (500x for tank test specimens, 1000x for anodic dissolution specimens) are representative of the coarse-grained supercritical HAZ microstructures (i.e. Figures 5, 7, 9, 11, 13, 15, 17, 19, 21, 23, 25, 27, 29, 31 and 33).

4.1.1 Profilometry and Macrosections

The profilometry measurements made in the previous program[1] are included in Appendix I. These measurements may be compared with the observations made from metallographic sections as summarized in Table 5.

The greatest discrepancies were found for samples exhibiting what has been termed HAZ/baseplate corrosion in which a distinct step is noted between the weld metal and the adjacent HAZ with no apparent step back up in baseplate. In general, the carbon-manganese steels at high heat inputs appear to show this type of attack as does steel B at higher heat inputs.

When there is coarse grained HAZ corrosion adjacent to the fusion line in combination with weld metal corrosion, the profilometry trace will not reflect the HAZ corrosion. For instance, specimens B21 and E31 both show some HAZ attack along with weld metal attack (Figures 26a and 30a), and yet the profilometry results in Appendix I do not indicate any HAZ attack. This small amount of HAZ attack may be of little practical significance when compared to the extent of adjacent weld metal corrosion, but it is still of interest when attempting to characterize the corrosion behaviour of different types of steels.

4.1.2 HAZ Microstructural Examination

To clarify the microstructural descriptions in the subsequent sections, a brief description of each of the broad categories is given below. These categories are those designated by the Welding Institute U.K.[4].

On a macro level, there are four general categories as the distance from the fusion boundary increases. The coarse grained supercritical HAZ next to the fusion line has been heated to a temperature sufficient to allow rapid austenite grain growth, typically above 1000°C. The fine grained supercritical HAZ has been heated above AC_3 but not high enough to allow rapid austenite grain growth. The intercritical HAZ has been heated between AC_1 and AC_3 resulting in partial transformation to austenite along with

substantial grain refinement. The subcritical HAZ has been heated to a maximum temperature less than AC_1. Pearlite is often spheroidised in this region but otherwise it is very similar to baseplate structure.

There are six principal microstructural constituents in the coarse grained supercritical HAZ. These are described below.

Martensite (M), although generally promoted by increased alloy content, also occurs in carbon-manganese steels when cooling is very rapid.

Ferrite with martensite, austenite and carbides (MAC) is generally the predominant microstructural constituent in C-Mn steels. This includes Widmanstatten ferrite associated with grain boundaries.

Intragranular Widmanstatten ferrite (WF) resembles the acicular ferrite constituent commonly seen in weld metal. It can be distinguished from ferrite with MAC by the small aspect ratio of the ferrite laths and the "basket-weave" appearance. This type of ferrite forms at higher transformation temperatures and is generally associated with slower cooling rates.

Pro-eutectoid ferrite (PF) generally formed at prior austenite grain boundaries, is often associated with higher heat inputs and low alloy content.

Ferrite-Carbide aggregate (FC) appears in regions away from grain boundaries and is a result of the eutectoid decomposition reaction. It appears as a dispersion of carbides in ferrite at high magnification. Also included in this category is pearlite which is generally associated with very high heat input. It is sometimes difficult to distinguish pearlite from ferrite-carbide aggregate even at high magnification. However, one difference is that pearlite in the HAZ is often associated with grain boundaries[4].

Table 6 gives a visual assessment of the approximate proportions of each of the microstructural constituents found for each specimen examined.

Low Heat Input

At lower heat inputs steels B, F and J show similar microstructures containing some martensite and relatively fine ferrite with aligned MAC, most of which is related to Widmanstatten ferrite sideplates associated with pro-eutectoid ferrite at the grain boundaries (See Figures 15, 25 and 29).

Steels C, G and H also show similar microstructures consisting predominantly of ferrite with MAC (both aligned and non-aligned). The carbides are blunter and much coarser than those in the other steels (See Figures 13, 19 and 23).

Steels A and D have similar microstructures showing less needlelike laths of MAC than B, F and J. As well, there are regions of ferrite containing fine dispersions of carbides which become relatively dense at some locations (See Figures 5 and 7).

At low heat input, steels E and K have their own relatively unique microstructures. Although not dissimilar to steel C, E does have the unique feature of grain boundaries darkly outlined by carbides (Figures 31 and 33). Steel K contains pro-eutectoid ferrite even at the lowest heat input and there are a number of sideplates associated with these. There are large dark etching regions which appear to be a fine dense dispersion of carbides in ferrite (Figures 9 and 11).

High Heat Input

At higher heat inputs the trends are similar with some minor changes.

Steels A and D are still similar, but at high heat inputs, steel K also fits in with these. The microstructures are similar to the lower heat input structure for K steel with the coarseness of the grain boundary ferrite and associated sideplates increasing as the heat input increases (See Figures 5, 7 and 9).

Steels F, J and B are also still grouped together but at higher heat inputs, steel H also fits in with these. The microstructures

are predominantly coarse MAC with some pro-eutectoid ferrite. Carbides are relatively random with some aligned and some non-aligned (See Figures 15, 23, 25 and 29).

Steels C and G have structures similar to F, J, B and H with the exception that the carbides are very coarse and blunt and there is very little pro-eutectoid ferrite present (See Figures 13 and 19).

Steel E (Figure 31) remains in a class by itself. There is a distinct coalescence of carbides and "fading" of the structure such as occurs upon stress-relief. Again, the grain boundaries show no primary ferrite but rather are darkened by the presence of carbides.

4.1.3 Corrosion with Microstructure

A comparison of the microstructural groupings with HAZ corrosion resistance is shown in Table 7. Generally speaking, the best HAZ corrosion resistance is seen for carbon-manganese steels with manganese levels of .75 to 1.10 while the worst HAZ corrosion resistance is seen for the microalloyed steels with manganese levels from 1.24 to 1.40.

Whether this effect is strictly related to composition or also the microstructure, is difficult to say since all poor performers have similar manganese levels, as well as similar microstructures.

It is apparent that sideplate type ferrite with MAC is not in itself detrimental to corrosion resistance since all three carbon manganese steels contain anywhere from 20 to 85% of this phase (dependent on heat input, see Table 6). However, it is possible that the coarse carbide, intragranular (i.e. not sideplates) ferrite with aligned/non-aligned MAC, may be more susceptible to corrosion, as this phase makes up about 80% of the microstructure in most of the susceptible specimens.

4.1.4 Selection of Specimens for Electron Microscopy

Six specimens were selected for electron microscopy based on the results of the optical microscopy.

The specimens selected include B31, B72, F31, F72, K31 and K72, all from the Tank Test specimens. B, F and K represent each of the categories of steel examined; that is, low alloy, microalloy and C-Mn, respectively. Steel F was one of the steels which showed the presence of a less attacked intercritical region of the HAZ in comparison to the super and subcritical regions. 31 and 72 conditions were chosen to represent low and high heat inputs, respectively. The results of the electron microscopy are presented in the second volume to this report.

4.2 Hardness Measurements

Table 8 lists the hardness measurements for each region of the heat affected zone for each of the steels examined.

4.2.1 Corrosion with Hardness

Figures 34 and 35 show that the depth of attack in the coarse grained HAZ appears to increase up to a hardness of about 225 HV_{10} and then reaches a plateau for both the Tank and Anodic Dissolution Test. This is similar to the results of a concurrent program[5].

The significance of this finding is somewhat nebulous, as higher hardnesses are achieved through addition of hardening elements such as manganese. As already well documented, increasing manganese increases susceptibility to HAZ corrosion[1,6]. For instance, the steel having the best corrosion resistance (Steel K) has the lowest coarse grain HAZ hardness. This low hardness, in light of the higher carbon content, must be due to the lack of other hardening elements. As well, the steels having CG HAZ hardness above the 225 HV_{10} plateau (B,E,F,G,H and J), with the exception of E, generally have manganese contents of 1.1 or greater although B is borderline. E is an exceptional case as it has quite high nickel and copper contents.

4.3 Corrosion with Heat Input

The relationship between heat input and depth of attack, which was established by Scandinavian investigators[6], seems to be verified with the extent of corrosion at any particular heat input determined by manganese content as shown in Figure 36.

5.0 SUMMARY

Complete metallographic examination of corrosion test specimens has shown the following.

1. Carbon-manganese steels are less susceptible to preferential HAZ corrosion than alloyed or microalloyed grades.

2. Where HAZ corrosion does occur in C-Mn steels, it is generally only the supercritical region of the HAZ which is attacked.

3. The microstructures associated with the CG HAZ of these steels consists predominantly of sideplate ferrite associated with pro-eutectoid ferrite at the grain boundaries as well as large dark etching regions which are fine dense dispersions of carbides.

4. The microalloyed steels are very susceptible to HAZ corrosion.

5. HAZ corrosion occurs in the microalloyed steels throughout the HAZ. For steels F and G, the whole HAZ corrodes with the exception (in some cases) of the intercritical region. In other cases, there is general HAZ/baseplate corrosion, particularly at higher heat inputs.

6. The microstructure associated with the CG HAZ of these steels consists of predominantly ferrite with MAC (both aligned and non-aligned) in the form of very coarse carbides.

ACKNOWLEDGEMENTS

The author wishes to thank the following people for their valuable contributions to this report.

1. L. Laurin, M. Chambers and L. Thompson for specimen preparation and experimental work.
2. D. Perrin for report preparation.
3. R. Brigham at CANMET/PMRL for supplying Tank test specimens.
4. G. Weatherly at the University of Toronto for performing electron microscopy.
5. D.S.S. for funding under a 50/50 cost-shared program.
6. Algoma Steel Corp. Ltd. for additional funding.

REFERENCES

1. Donepudi, V.S., Santyr, S., Malik, L., Garner A.J., and McLean, M. "Evaluation of Weld Zone Corrosion of Shipbuilding Steel Plates for Use in the Arctic Environment", DSS File No: 57SZ.T8080-4-6737, December 1986.

2. Brigham, R. "Corrosion of Welds in Icebreaking Ships", CANMET Report No. 86-66(OP-J), July 1986.

3. Brigham, R. Personal communication.

4. The Welding Institute slide series on Weld and HAZ Microstructures (1984).

5. Santyr, S., Malik, L., and Donepudi, V.S. "Assessment of Weld Corrosion on the MV Arctic", report submitted to CFER, December 1986.

6. Gilmour, J.B. "The Corrosion of Welds in Icebreaking Ships - A Review", CANMET Report No. 80-14E, Energy, Mines and Resources Canada, April 1980.

TABLE 1: CHEMICAL COMPOSITION OF BASEPLATE MATERIALS

	C	Mn	Si	P	S	Cu	Ni	Cr	Mo	V	Ti	Nb	Al
A (300W)	.16	1.10	.19	.014	.012	---	---	---	---	----	----	----	.033
B (350AT)	.16	1.08	.32	.013	.006	.30	.57	.38	---	----	----	----	.051
C (350WT)	.10	1.24	.23	.012	.010	.05	.07	.04	---	.044	----	.039	.051
D (260WT)	.16	1.01	.23	.023	.019	---	---	---	---	----	----	----	.042
E (A710 Gr. A, Cl 3)	.06	.54	.29	.005	.005	1.20	.89	.70	.21	----	----	.037	----
F (Algoma LT60)	.12	1.39	.28	.017	.011	.15	.15	.17	---	.053	----	.041	.027
G (Stelco 350WT)	.07	1.40	.29	----	.004	___	.25	.25	---	.08	.012	.02	----
H (Stelco)	.15	1.40	.29	.009	.005	---	.27	---	---	.07	.011	----	----
J (EH36)	.15	1.45	.45	.016	.006	.14	---	---	---	.031	----	----	.022
K (A36)	.20	.75	.03	.015	.019	---	---	---	---	----	----	----	----
L (Shoralsim 355Z)	.11	1.24	.42	.011	.005	.30	.16	.08	---	----	----	----	.030

TABLE 2: CHEMICAL COMPOSITION OF WELD METALS

	C	Mn	Si	P	S	Cu	Ni	Cr	Mo	V	Ti	Al	B
1 SMAW OK73.08	.055	1.16	.37	.01	.010	.35	.55	.065	---	.030	--	.005	---
2 SMAW E7018-1	.050	1.40	.37	.01	.013	.035	.05	.04	---	.010	--	.005	---
3 SMAW E8018-C1	.035	0.81	.30	.008	.015	.026	2.15	.025	---	.015	--	.005	---
4 SMAW E8018-W	.040	.96	.38	.01	.012	.185	1.40	.245	---	.015	--	.005	---
5 SAW L60/761	.035	1.85	1.12	.025	.020	.065	.02	.045	---	----	--	.005	---
6 SAW SD2-3Ni/OP121TT	.060	.95	.27	.01	.005	.085	2.79	.125	.11	----	--	.015	---
7 SAW Tibor 22/OP121TT	.055	1.01	.17	.02	.005	.165	.06	.095	.24	----	--	.013	.0007
8 SAW Thyssen S3Nil/	.085	1.16	.22	.013	.010	.065	1.23	.035	---	.010	--	.015	---

TABLE 3: TANK TEST SPECIMENS FOR EXAMINATION

Identification	Steel	Consumable	Process	Heat Input (kJ/mm)
B21	350AT	7018-1	SMAW	1.2
B31	350AT	8018-C1	SMAW	1.2
B32	350AT	8018-C1	SMAW	2.5
B61	350AT	SD2-3Ni/OP121TT	SAW	2.5
B62	350AT	SD2-3Ni/OP121TT	SAW	4.0
B71	350AT	Tibor 22/OP121TT	SAW	2.5
B72	350AT	Tibor 22/OP121TT	SAW	4.0
E31	A710 Gr A, C13	8018-C1	SMAW	1.2
E62	A710 Gr A, C13	SD2-3Ni/OP121TT	SAW	4.0
F21	LT60	7018-1	SMAW	1.2
F31	LT60	8018-C1	SMAW	1.2
F32	LT60	8018-C1	SMAW	2.5
F61	LT60	SD2-3Ni/OP121TT	SAW	2.5
F62	LT60	SD2-3Ni/OP121TT	SAW	4.0
F71	LT60	Tibor 22/op121TT	SAW	2.5
F72	LT60	Tibor 22/OP121TT	SAW	4.0
G31	350WT	8018-C1	SMAW	1.2
G62	350WT	SD2-3Ni/OP121TT	SAW	4.0
K21	A36	7018-1	SAW	1.2
K31	A36	8018-C1	SMAW	1.2
K71	A36	Tibor 22/OP121TT	SAW	2.5
K72	A36	Tibor 22/OP121TT	SAW	4.0

TABLE 4: ANODIC DISSOLUTION TEST SPECIMENS FOR EXAMINATION

Identification	Steel	Consumable	Process	Heat Input (kJ/mm)
A31	300W	8018-C1	SMAW	1.2
B31	350AT	8018-C1	SMAW	1.2
CR31	350WT	8018-C1	SMAW	1.2
D31	260WT	8018-C1	SMAW	1.2
E31	A710 Gr A, C13	8018-C1	SMAW	1.2
F31	LT60	8018-C1	SMAW	1.2
G31	350WT	8018-C1	SMAW	1.2
H31	350WT	8018-C1	SMAW	1.2
J31	EH36	8018-C1	SMAW	1.2
K31	A36	8018-C1	SMAW	1.2
A62	300W	SD2-3Ni/OP121TT	SAW	4.0
B62	350AT	SD2-3Ni/OP121TT	SAW	4.0
CR6	350WT	SD2-3Ni/OP121TT	SAW	4.0
D62	260WT	SD2-3Ni/OP121TT	SAW	4.0
E62	A710 Gr A, C13	SD2-3Ni/OP121TT	SAW	4.0
F62	LT60	SD2-3Ni/OP121TT	SAW	4.0
G62	350WT	SD2-3Ni/OP121TT	SAW	4.0
H62	350WT	SD2-3Ni/OP121TT	SAW	4.0
J62	EH36	SD2-3Ni/OP121TT	SAW	4.0
K62	A36	SD2-3Ni/OP121TT	SAW	4.0
B21	350AT	7018-1	SMAW	1.2
F21	LT60	7018-1	SMAW	1.2
B61	350AT	SD2-3Ni/OP121TT	SAW	2.5
F61	LT60	SD2-3Ni/OP121TT	SAW	2.5
B71	350AT	Tibor 22/OP121TT	SAW	2.5
F71	LT60	Tibor 22/OP121TT	SAW	2.5
K71	A36	Tibor 22/OP121TT	SAW	2.5

TABLE 5: METALLOGRAPHIC OBSERVATIONS MADE FROM MACROSECTIONS

I.D.	Anodic Dissolution	Tank Test
Carbon-Manganese Grades:		
SMAW		
A31	HAZ attack - predominantly supercritical but extending into intercritical region (Figure 4a)	
D31	HAZ attack - predominantly supercritical but gradual rise to baseplate around subcritical region (Figure 6a)	
K21		WM attack associated with very slight supercritical HAZ attack (Figure 10a)
K31	Very slight supercritical HAZ attack ending at intercritical region (Figure 8a)	Some WM attack but also supercritical HAZ attack ending at FG-supercritical/ intercritical interface (Figure 10b)
SAW		
A62	HAZ/baseplate attack - predominantly supercritical but very gradual rise to surface (Figure 4b)	
D62	HAZ/baseplate attack - predominantly supercritical but very gradual rise to surface (Figure 6b)	
K62	HAZ/baseplate attack - as with A62 and D62, but different to determine where corrosion ends (Figure 8b)	
K71	No discernible attack in HAZ (Figure 8c)	Supercritical HAZ attack - could be mechanical effect (Figure 10c)
K72		No discernible attack in HAZ (Figure 10d)

.../continued

TABLE 5...continued

I.D.	Anodic Dissolution	Tank Test
Microalloyed Grades:		
SMAW		
C31	HAZ attack - deepest in supercritical HAZ with gradual rise to surface just beyond subcritical HAZ (Figure 12a)	
F21	Coarse grained HAZ attack associated with weld metal attack. Attack ends at interface between inter-critical and subcritical HAZ (Figure 14a)	Deep coarse grained HAZ attack associated with weld metal attack. Similar to anodic specimen (Figure 16a)
F31	Whole HAZ attack i.e. relatively uniform depth from fusion line to just beyond visible subcritical HAZ (Figure 14b)	Whole HAZ attack similar to anodic specimen (Figure 16b)
F32		Coarse grained HAZ attack - could be confused by mechanical effects (Figure 16c)
G31	HAZ attack - deepest in supercritical and subcritical HAZ regions (Figure 18a)	Severe whole HAZ attack (Figure 20a)
H31	Whole HAZ attack as in F31 (Figure 22a)	
J31	Whole HAZ attack similar to F31 (Figure 24a)	
SAW		
C62	Very slight HAZ/baseplate attack (Figure 12b)	
F61	Very slight HAZ/baseplate attack (Figure 14c)	HAZ attack - deepest in supercritical and subcritical HAZ, high surface roughness (Figure 16d)

.../continued

TABLE 5...continued

I.D.	Anodic Dissolution	Tank Test
F62	HAZ attack - deepest in supercritical HAZ with gradual rise to surface just beyond visible subcritical HAZ (Figure 14d)	HAZ attack - no real relief in baseplate (Figure 16e)
F71	HAZ attack - deepest in supercritical HAZ with gradual rise to surface just beyond visible subcritical HAZ (Figure 14e)	Deep, rounded HAZ attack - appears to be mechanical in nature (Figure 16f)
F72		May be HAZ attack - high surface roughness interferes with assessment (Figure 16g)
G62	HAZ attack - deepest in supercritical HAZ and just beyond visible, subcritical HAZ (Figure 18b)	Severe whole HAZ attack (Figure 20b)
H62	Whole HAZ attack - very gradual rise to surface, difficult to determine where corrosion ends (Figure 22b)	
J62	Slight HAZ attack - deepest in supercritical HAZ, gradual rise to surface (Figure 24b)	
Alloyed Grades:		
SMAW		
B21	Supercritical HAZ attack ending at intercritical region, associated with weld metal attack (Figure 26a)	Appears to be weld metal attack only (Figure 28a)
B31	Very slight, whole HAZ attack (Figure 26b)	Slight, HAZ/baseplate attack (Figure 28b)

.../continued

TABLE 5...continued

I.D.	Anodic Dissolution	Tank Test
B32 (left)		Whole HAZ attack (Figure 28c)
E31	Supercritical HAZ attack ending at intercritical/ subcritical HAZ associated with weld metal attack (Figure 30a)	HAZ attack - deepest in supercritical and subcritical HAZ (Figure 32a)
SAW		
B61	HAZ attack - deepest in supercritical HAZ with very gradual rise to surface well beyond visible HAZ (Figure 26c)	Severe HAZ attack - deepest in supercritical HAZ (Figure 28e)
B62	Very slight HAZ/baseplate attack - deepest in supercritical (Figure 26d)	Severe HAZ attack - deepest in supercritical and subcritical HAZ (Figure 28f)
B71	Very slight HAZ/baseplate attack as in B62 (Figure 26e)	HAZ attack - predominantly supercritical HAZ - high surface roughness (Figure 28g)
B72		Deep, rounded HAZ attack - difficult to determine leading or trailing edge (Figure 28h and 28i)
E62	No discernible attack (Figure 30b)	HAZ attack - deepest in supercritical HAZ with "step" at intercritical region (Figure 32b)

TABLE 6: VISUAL ASSESSMENT OF MICROSTRUCTURAL CONSTITUENT PROPORTIONS FROM ANODIC DISSOLUTION SPECIMENS

I.D.	M	F(MAC)	WF	PF	FC
A31	--	85	--	5	10
A62	--	65	5	20	10
D31	--	77	20	--	3
D62	--	30	5	45	20
K21	--	60	--	10	30
K31	--	45	--	20	35
K62	--	20	--	35	45
K71	--	30	--	40	30
K72	--	30	--	40	30
C31	--	95	5	--	--
C62	--	88	10	2	--
F21	20	80	--	--	--
F31	15	85	--	--	--
F61	--	85	10	--	5
F62	--	85	10	2	3
F72	--	65	35	--	--
G31	--	80	20	--	--
G62	--	90	10	--	--
H31	--	83	10	2	5
H62	--	50	45	5	--
J31	10	90	--	--	--
J62	--	85	8	5	2
B21	20	75	--	5	--
B31	10	85	--	5	--
B32	5	90	--	5	--
B62	--	80	7	8	5
B71	--	75	10	5	10
B72	--	75	5	10	10
E31	5	90	2	--	--
E62	--	100	--	--	--

TABLE 7: RELATIVE HAZ CORROSION RESISTANCE FOR THE DIFFERENT STEEL TYPES

Heat Affected Zone Corrosion Resistance	Corrosion Test	
	Tank Test	Anodic Dissolution Test
Good	[1]K, [3]E, [3]B	[1]K, [1]D, [3]B, [1]A
Fair	[2]C	[2]C, [3]E
Poor	[2]F, [2]G	[2]F, [2]G, [2]H, [2]J

[1] C-Mn Steels (A, D, K)

[2] Microalloyed Steels (C, F, G, H, J)

[3] Alloy Steels (E, B)

TABLE 8: HARDNESS MEASUREMENTS IN SPECIFIC REGIONS OF THE HAZ

I.D.	Baseplate	Subcritical HAZ	Intercritical HAZ	FG-Supercritical HAZ	CG-Supercritical HAZ
A31 - Anodic	148	175	184	---	198
A62 - Anodic	143	151	158	---	172
D31 - Anodic	138	143	153	---	195
D62 - Anodic	132	142	161	---	198
K21 - Tank	139	---	160	---	196
K31 - Tank	141	149	163	168	183
K31 - Anodic	138	149	158	---	183
K62 - Anodic	126	139	142	153	165
K71 - Tank	124	135	143	152	163
K71 - Anodic	136	146	157	171	185
K72 - Tank	123	129	138	155	---
C31 - Anodic	153	170	185	---	193
C62 - Anodic	152	164	---	---	180
F21 - Tank	150	185	---	256	266
F21 - Anodic	162	182	197	228	233
F31 - Tank	151	189	---	240	245
F31 - Anodic	155	179	212	---	242
F32 - Tank	168	---	215	---	233
F61 - Tank	143	197	---	201	---
F61 - Anodic	---	183	210	243	253
F62 - Tank	142	159	168	185	193
F62 - Anodic	144	160	173	193	201
F71 - Tank	151	162	169	---	206
F71 - Anodic	157	175	180	218	221
F72 - Tank	149	165	189	191	193

.../continued

TABLE 8...continued

I.D.	Baseplate	Subcritical HAZ	Intercritical HAZ	FG-Supercritical HAZ	CG-Supercritical HAZ
G31 - Tank	157	---	192	224	228
G31 - Anodic	159	---	189	202	---
G62 - Tank	150	---	165	179	183
H31 - Anodic	162	---	195	---	216
H62 - Anodic	160	166	182	196	206
J31 - Anodic	157	---	188	---	216
J62 - Anodic	156	179	178	202	215
B21 - Tank	155	222	262	---	270
B21 - Anodic	169	183	216	247	283
B31 - Tank	158	248	---	266	287
B31 - Anodic	159	249	---	258	---
B32 - Tank	144	177	229	---	282
B61 - Tank	161	177	195	---	213
B61 - Anodic	165	---	203	221	243
B62 - Tank	154	176	193	---	197
B62 - Anodic	146	178	189	---	203
B71 - Tank	159	181	221	---	225
B71 - Anodic	159	203	221	236	270
B72 - Tank	155	163	175	200	---
E31 - Tank	217	254	212	---	233
E31 - Anodic	203	185	203	---	240
E62 - Tank	220	187	183	---	238
E62 - Anodic	---	180	196	209	---

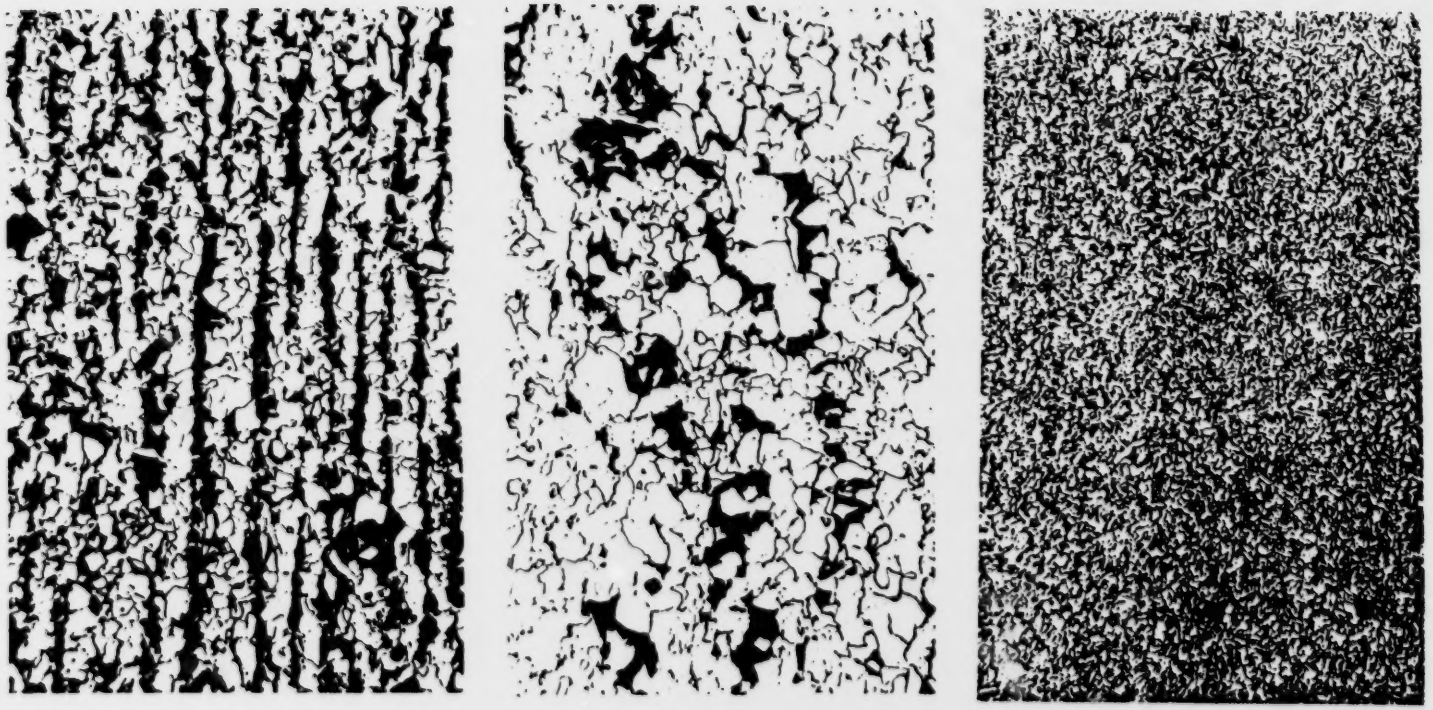

a b c

Figure 1: Baseplate microstructures for steels used in the Tank Test, Mag x200; Etch 2% Nital
a) B-350AT; Neg 9661 b) C-350WT; Neg 9090 c) E-A710, Gr. A, Cl3; Neg 9091

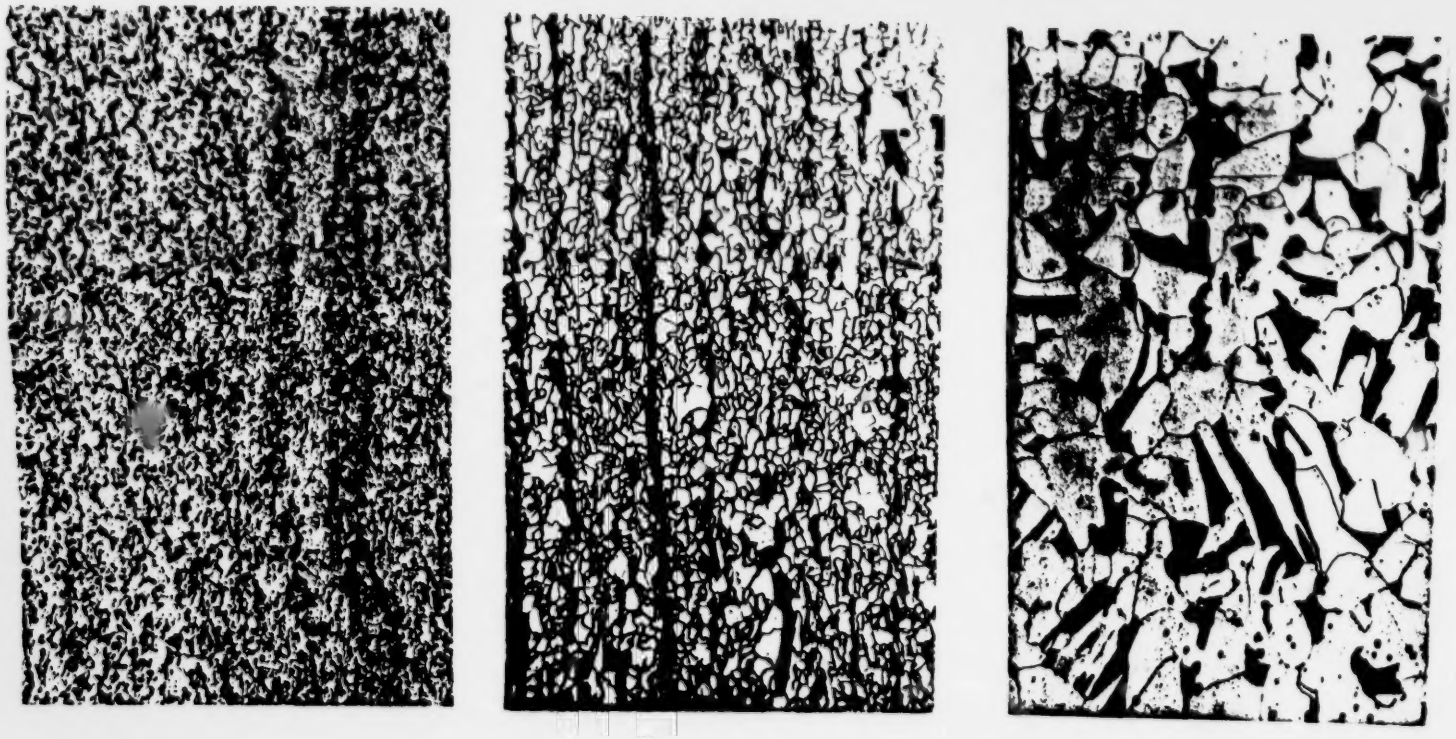

d e f

Figure 1 (continued): d) F-LT60; Neg 9093 e) G-350WT; Neg 9660 f) K-A36; Neg 9092

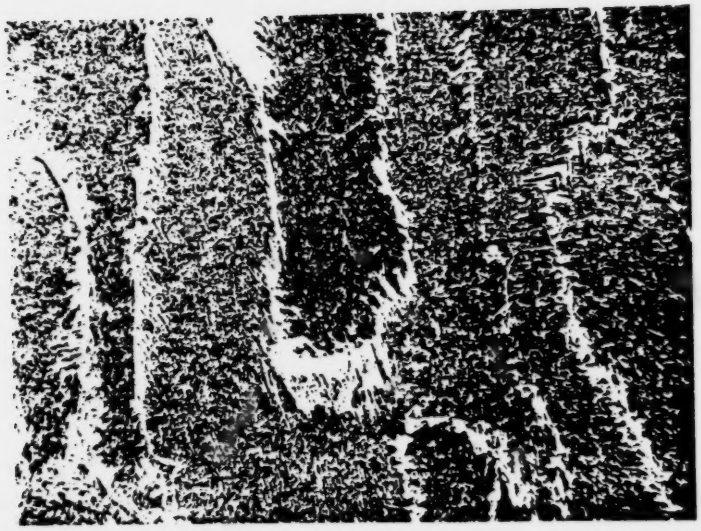

(a)

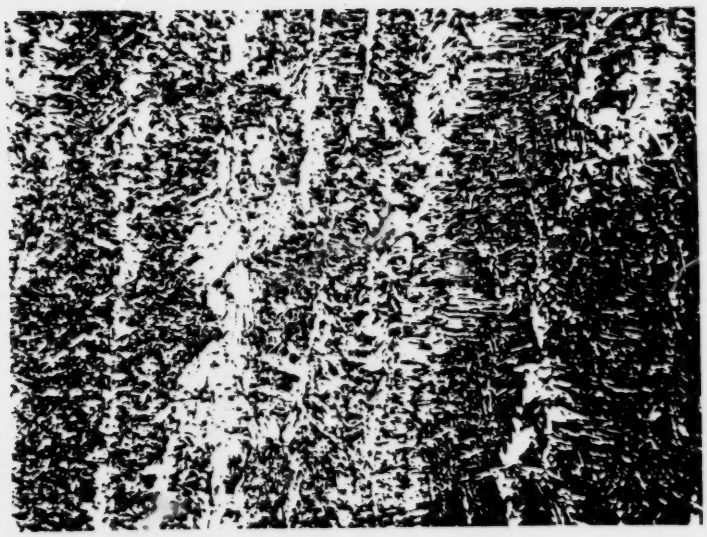

(b)

Figure 2: As-deposited SMAW weld metals, Mag x200; Etch 2% Nital
a) C-Mn type E7018-1, heat input 1.2 kJ/mm, Neg 9662
b) 2% Ni type E8018-C1, heat input 1.2 kJ/mm, Neg 9663

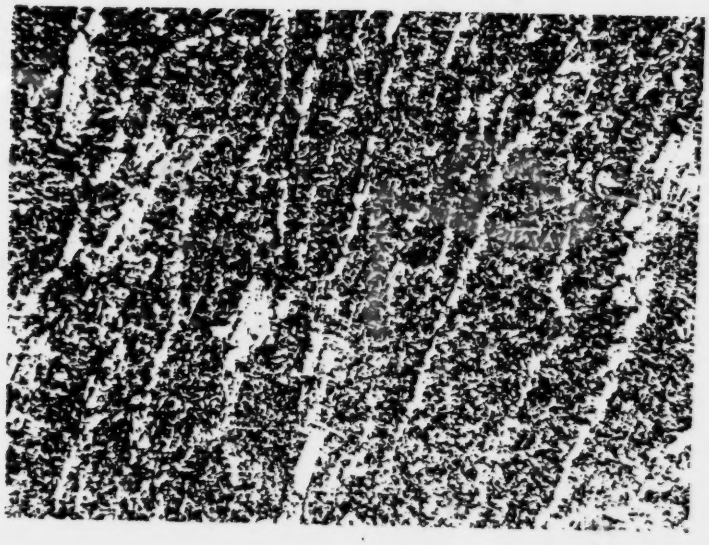

(a)

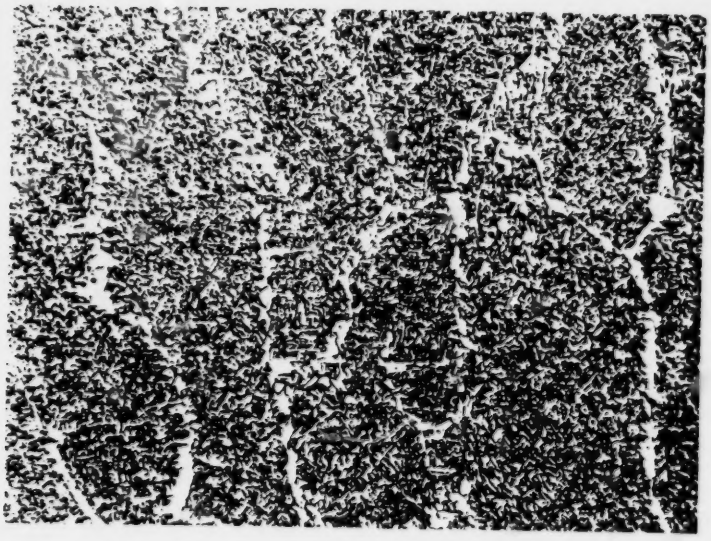

(b)

Figure 3: As-deposited SAW weld metals, Mag x200, Etch 2% Nital
a) 3% Ni type SD2-3Ni with Oerlikon 121TT flux, heat input 2.5 kJ/mm, Neg 9665
b) Tibor 22 with Oerlikon 121TT flux, heat input 2.5 kJ/mm, Neg 9667

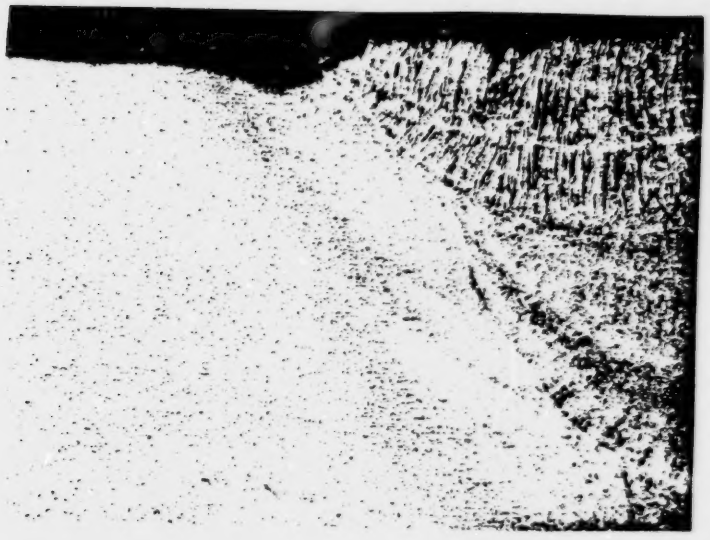

(a)

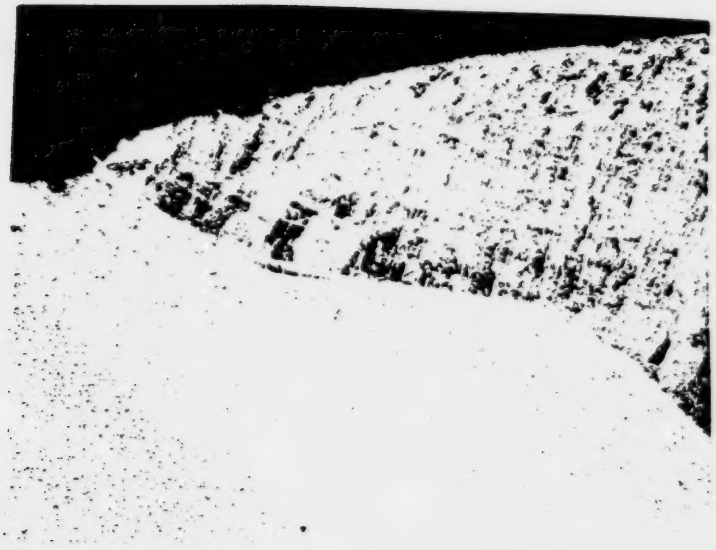

(b)

Figure 4: Steel A, Anodic Dissolution Test specimens, Mag x10, Etch 2% Nital
a) A31, Neg 9428 b) A62, Neg 9447

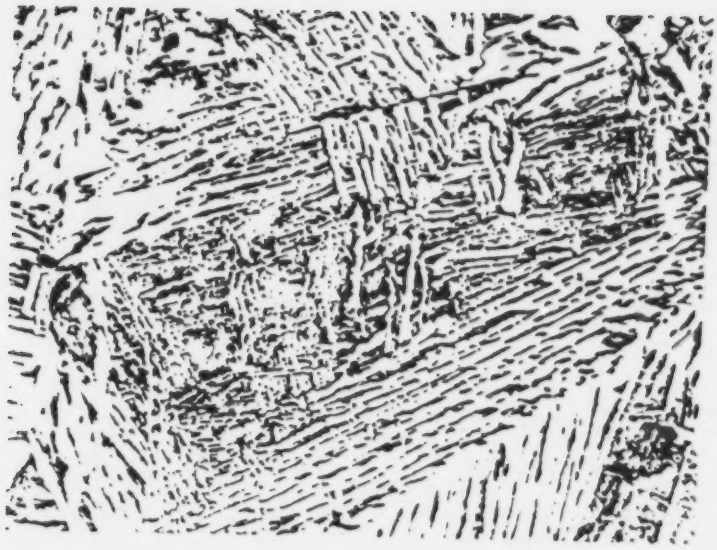

(a)

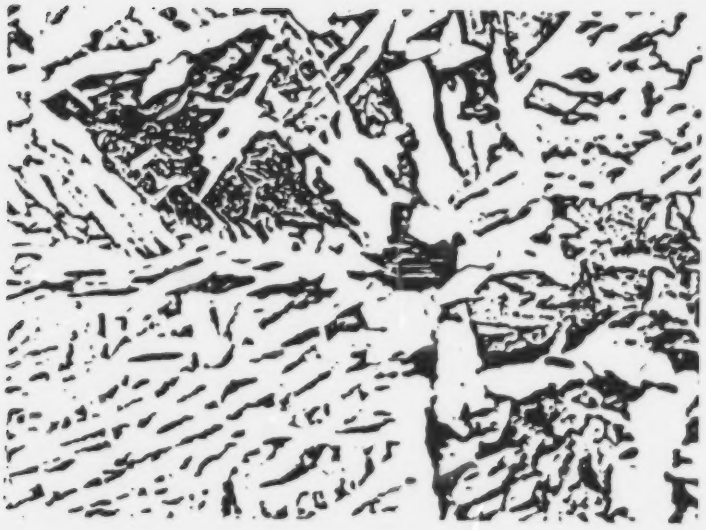

(b)

Figure 5: Steel A, Anodic Dissolution Test specimens, Mag x1000, Etch 2% Nital
a) A31, Neg 9787 b) Ao2, Neg 9800

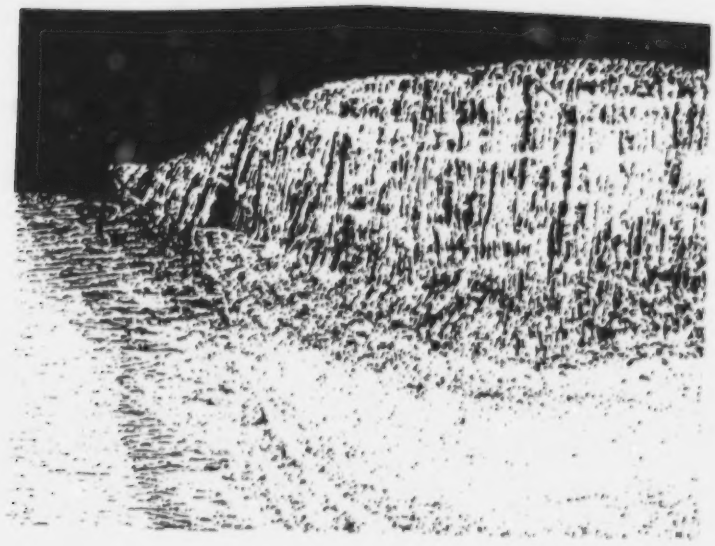

(a)

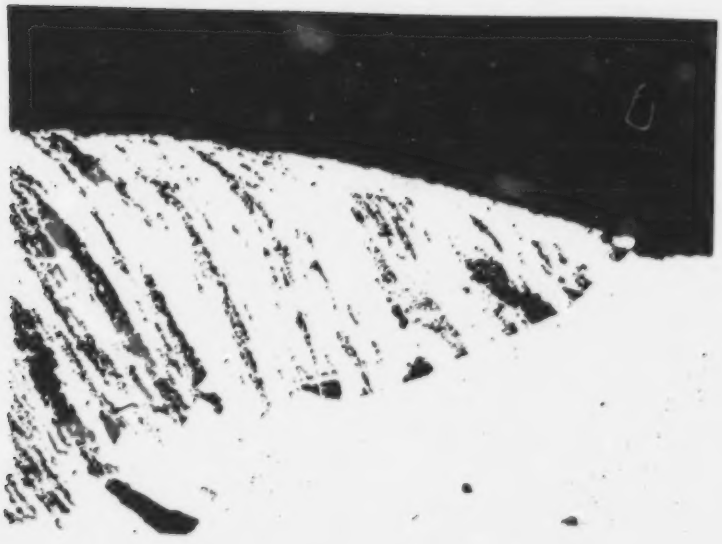

(b)

Figure 6: Steel D, Anodic Dissolution Test specimens, Mag x10, Etch 2% Nital
a) D31, Neg 9433 b) D62, Neg 9451

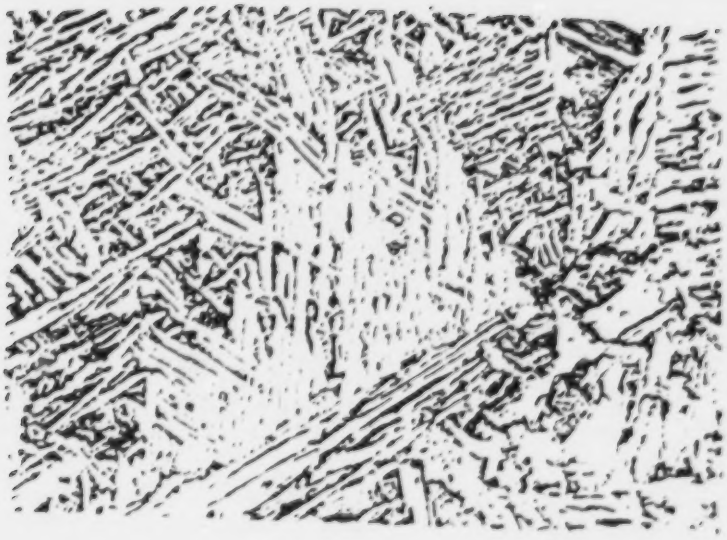

(a)

(b)

Figure 7: Steel D, Anodic Dissolution Test specimens, Mag x1000, Etch 2% Nital
a) D31, Neg 9811 b) D62, Neg 9803

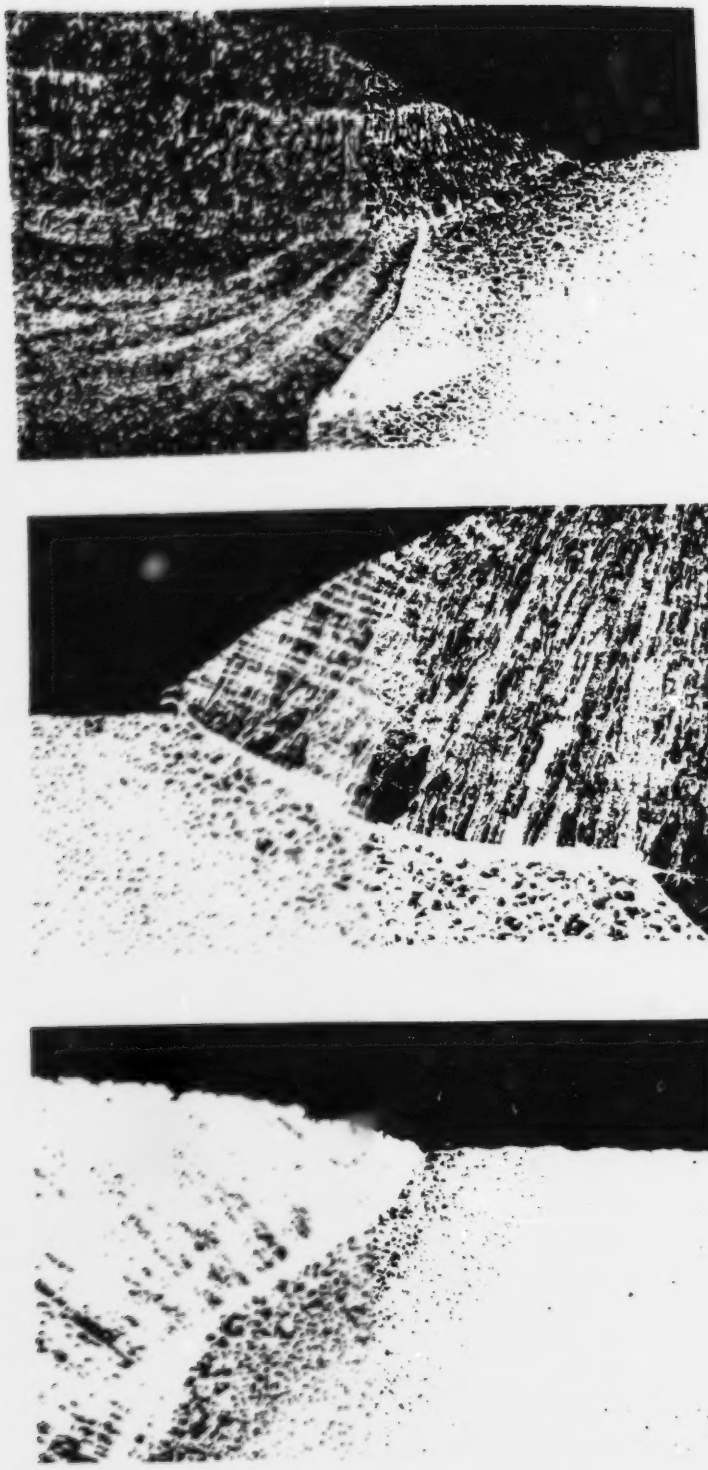

(a)

(b)

(c)

Figure 8: Steel K, Anodic Dissolution Test specimens, Mag x10, Etch 2% Nital
a) K31, Neg 9445 b) K62, Neg 9458 c) K71, Neg 9674

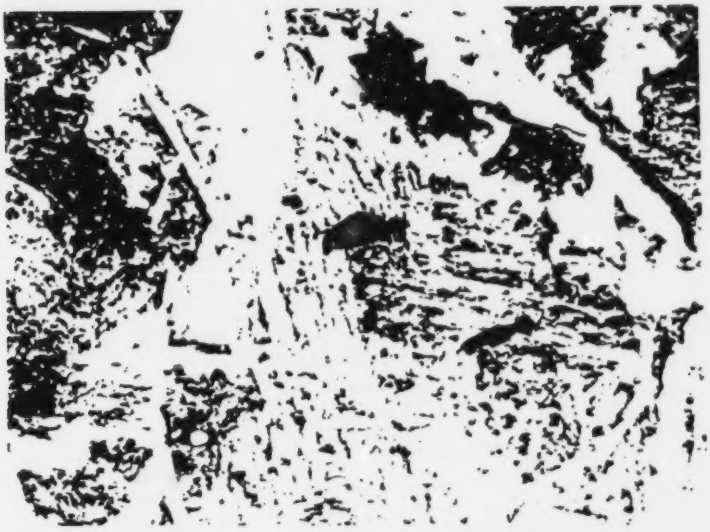

(a)

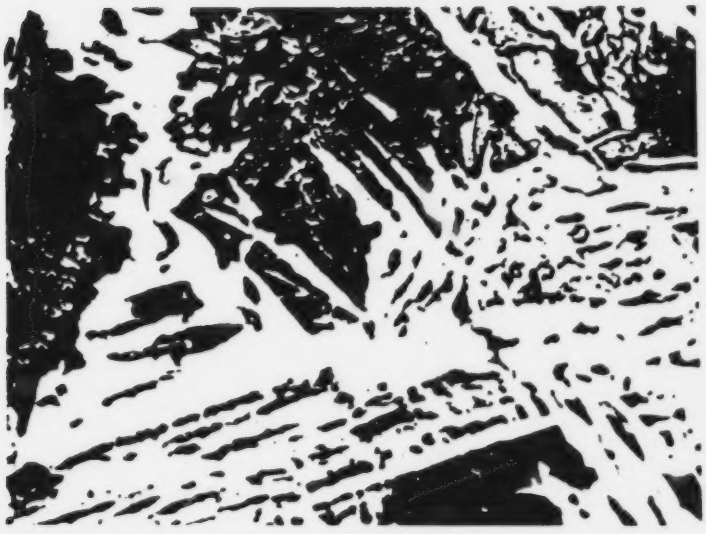

(b)

Figure 9: Steel K, Anodic Dissolution Test specimens, Mag x1000, Etch 2% Nital
a) K31, Neg 9799 b) K62, Neg 9809

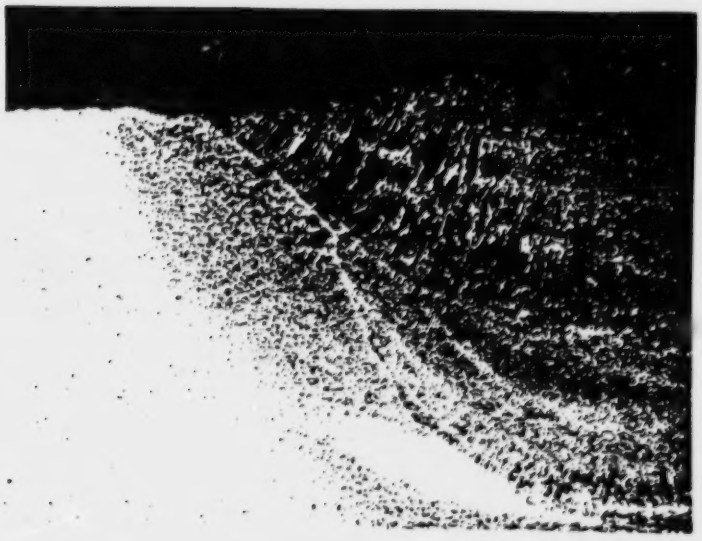

(a)

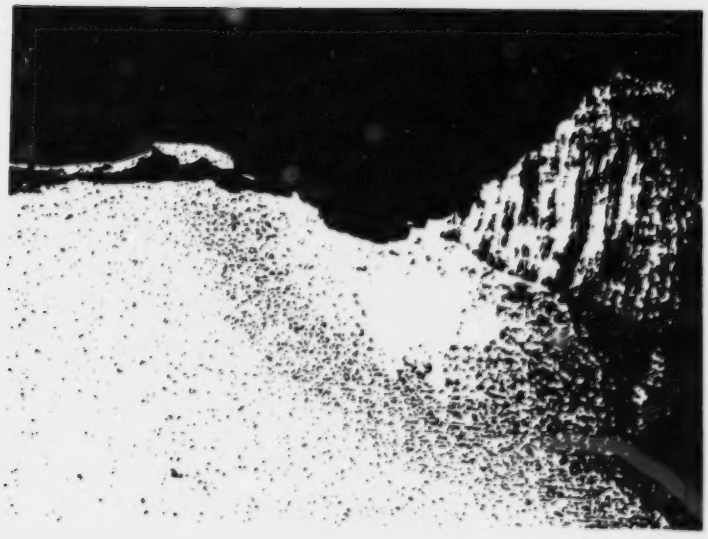

(b)

Figure 10: Steel K, Tank Test specimens, Mag x10, Etch 2% Nital
a) K21, Neg 9421, b) K31, Neg 9423

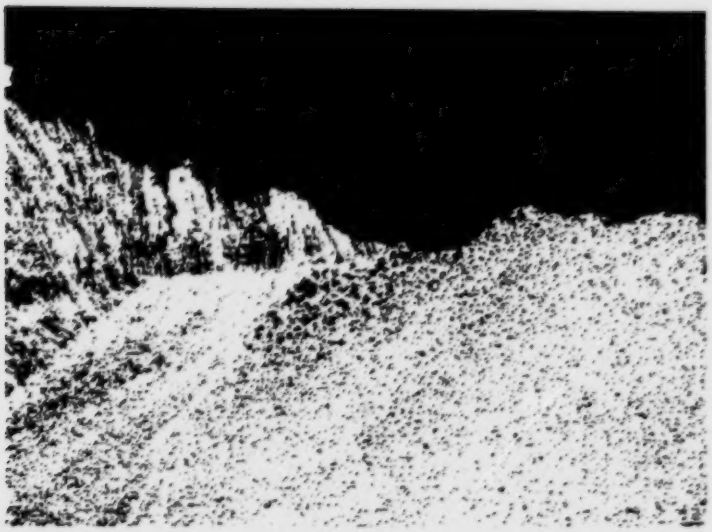

(c)

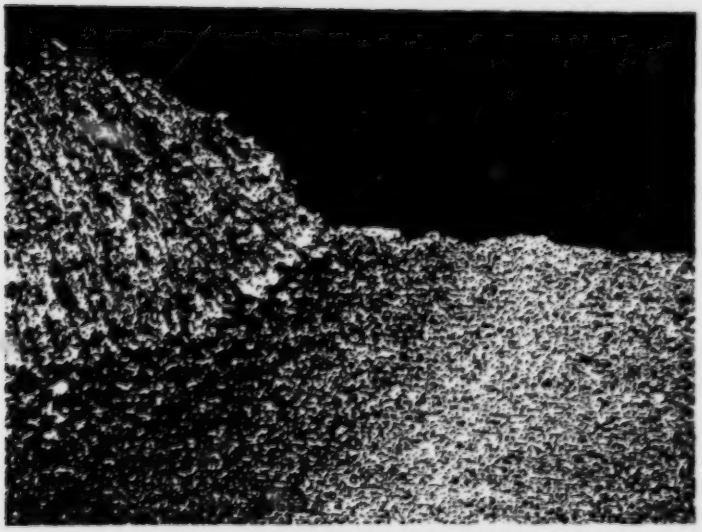

(d)

Figure 10 (continued): c) K71, Neg 9426 d) K72, Neg 9424

(a)

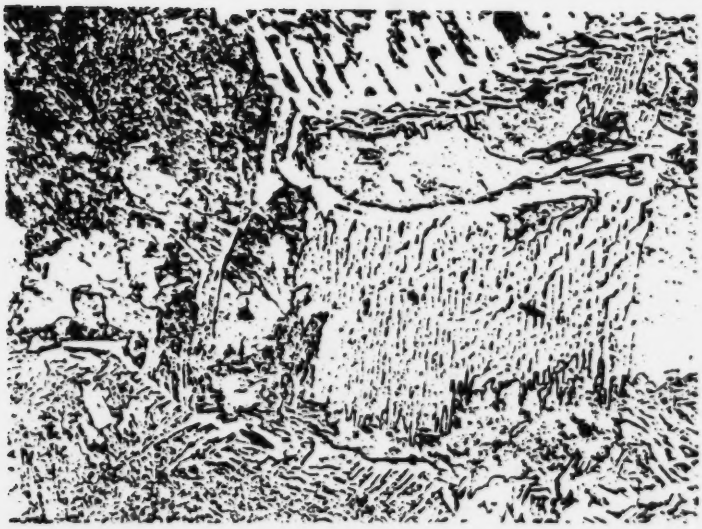

(b)

Figure 11: Steel K, Tank Test specimens, Mag x500, Etch 2% Nital
a) K21, Neg 9656 b) K31, Neg 9657

(c)

(d)

Figure 11 (continued): c) K71, Neg 9658 d) K72, Neg 9659

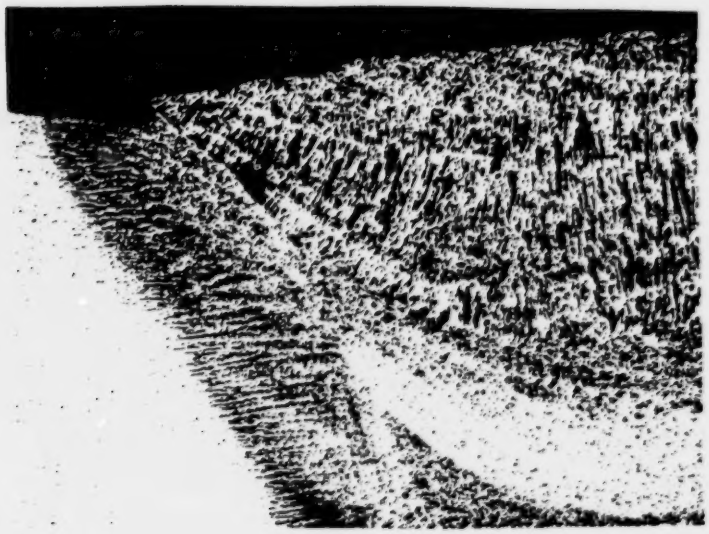

(a)

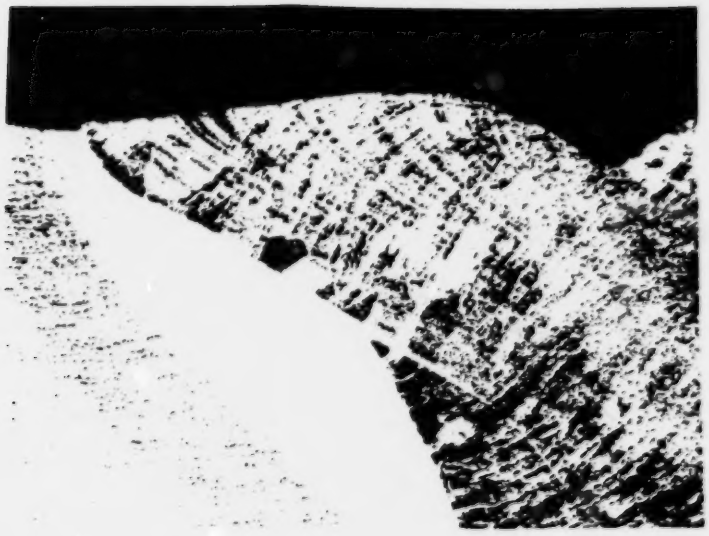

(b)

Figure 12: Steel C, Anodic Dissolution Test specimens, Mag x10, Etch 2% Nital
a) C31, Neg 9431 b) C62, Neg 9450

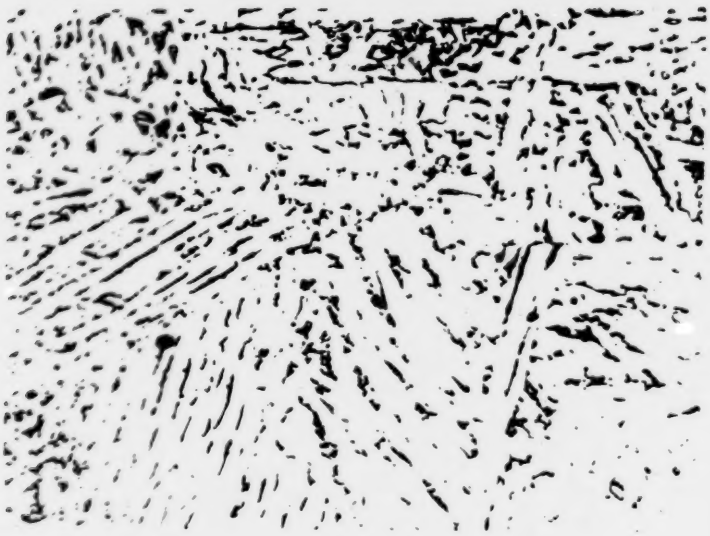

(a)

(b)

Figure 13: Steel C, Anodic Dissolution Test Specimens, Mag x1000, Etch 2% Nital; a) C31, Neg 9790 b) C62, Neg 9813

(a)

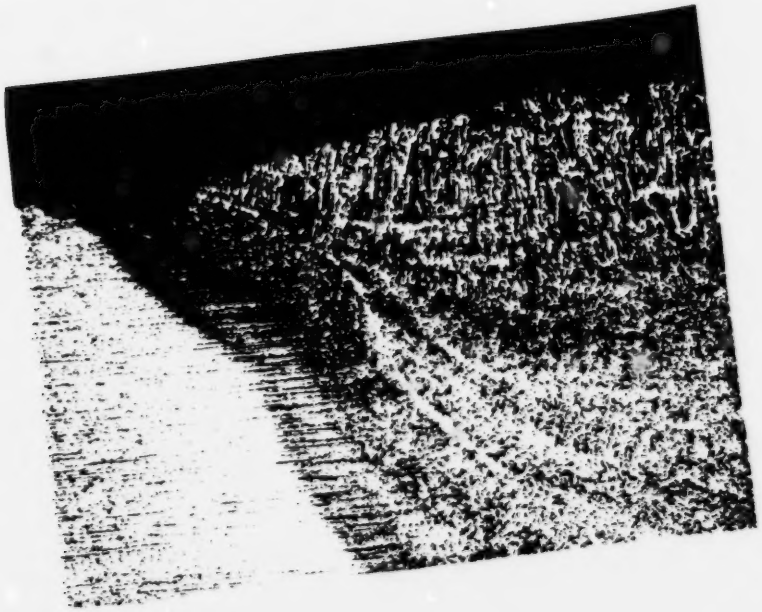

(b)

Figure 14: Steel F, Anodic Dissolution Test specimens, Mag x10, Etch 2% Nital
a) F21, Neg 9461 b) F31, Neg 9437

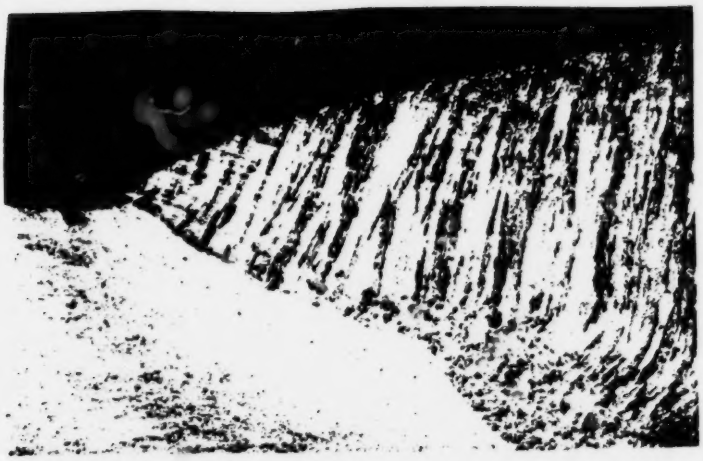

(c)

(d)

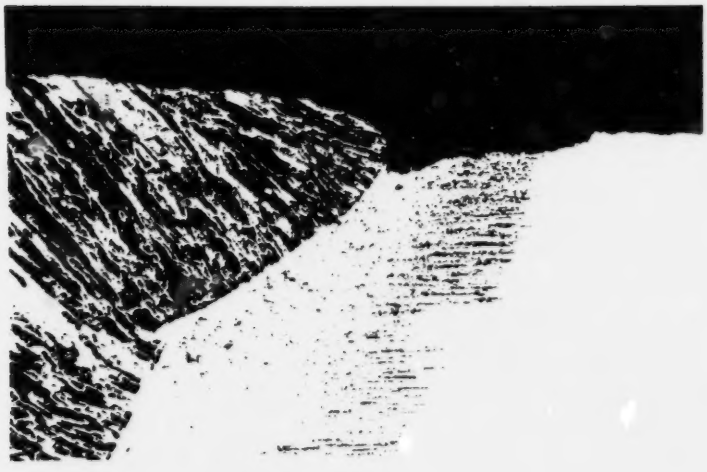

(e)

Figure 14 (continued): c) F61, Neg 9463 d) F62, Neg 9453, c) F71, Neg 9710

(a)

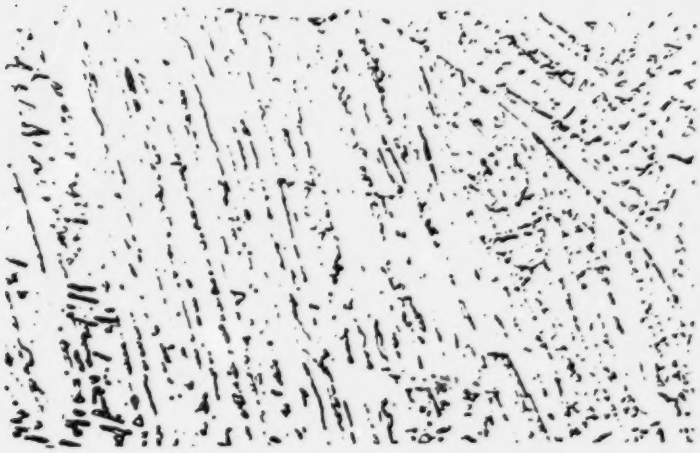

(b)

(c)

Figure 15: Steel F, Anodic Dissolution Test specimens, Mag x1000, Etch 2% Nital; a) F31, Neg 9795 b) F61, Neg 9821 c) F62, Neg 9805

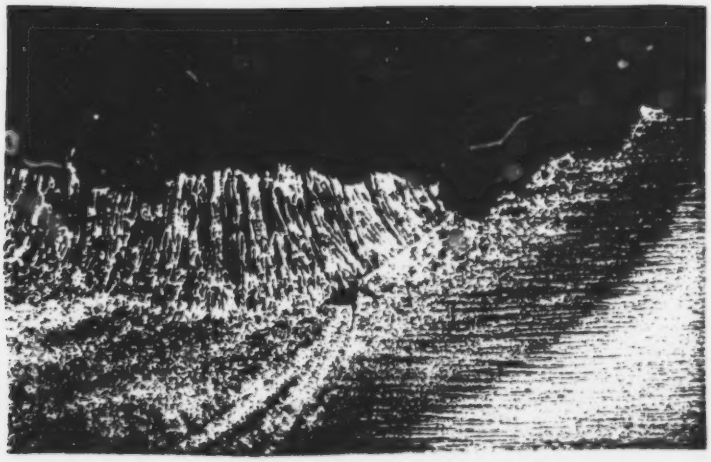

(a)

(b)

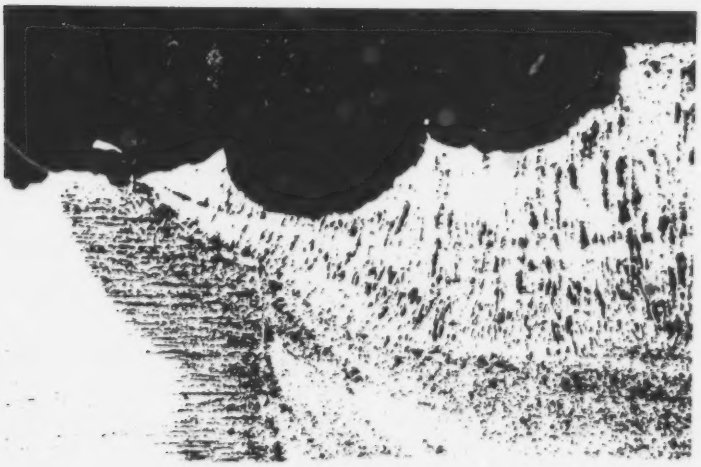

(c)

Figure 16: Steel F, Tank Test specimens, Mag x10, Etch 2% Nital
a) F21, Neg 9339 b) F31, Neg 9341 c) F32, Neg 9342

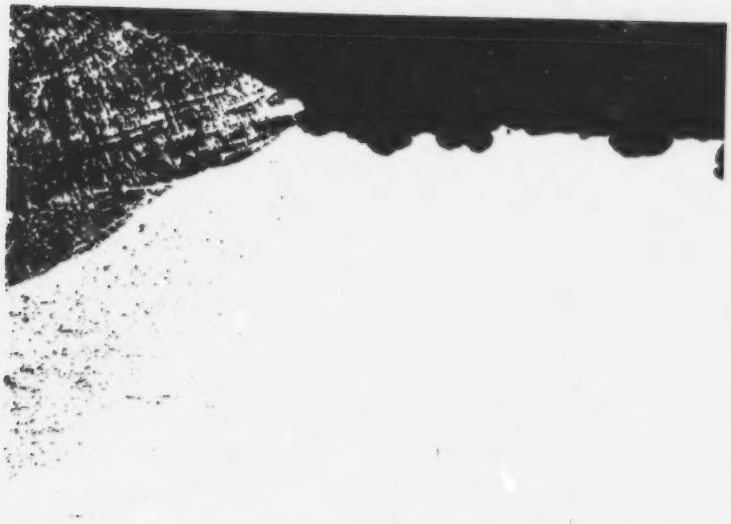

(d)

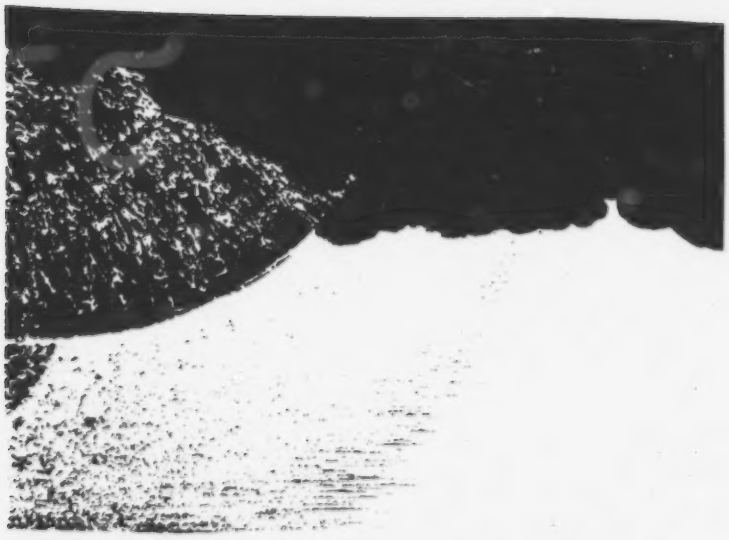

(e)

Figure 16 (continued): d) F61, Neg 9344 e) F62, Neg 9346

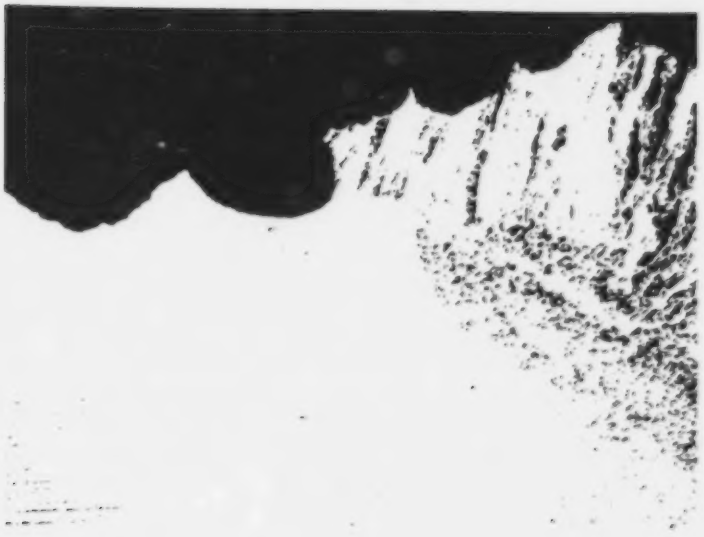

(f)

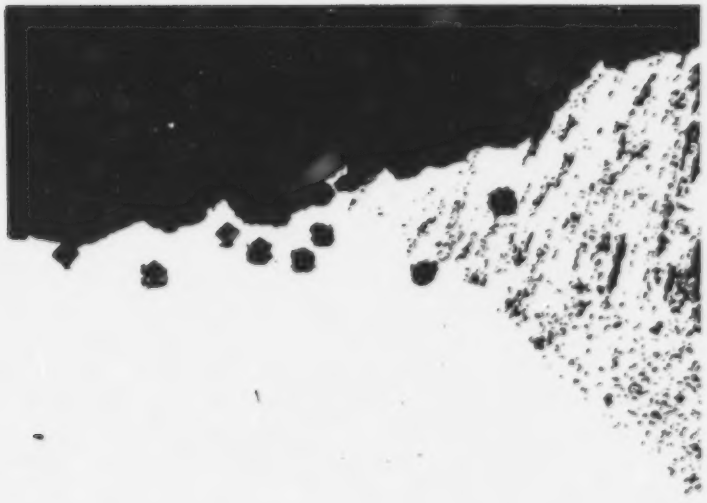

(g)

Figure 16 (continued): f) F71, Neg 9348 g) F72, Neg 9670

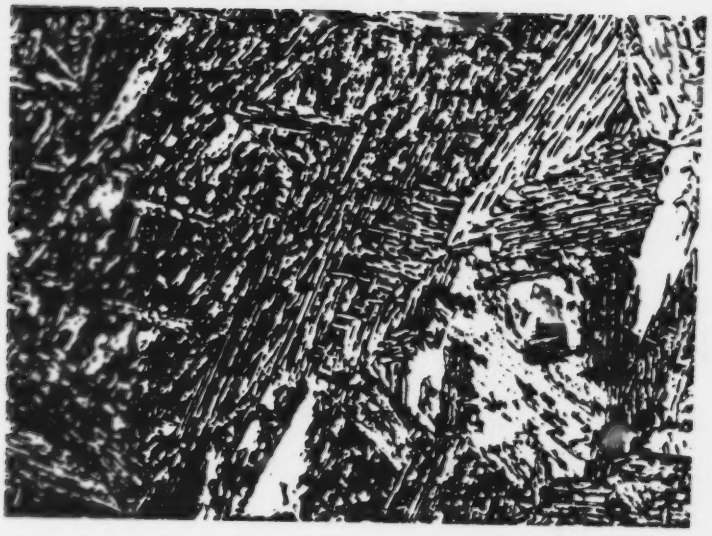

(a)

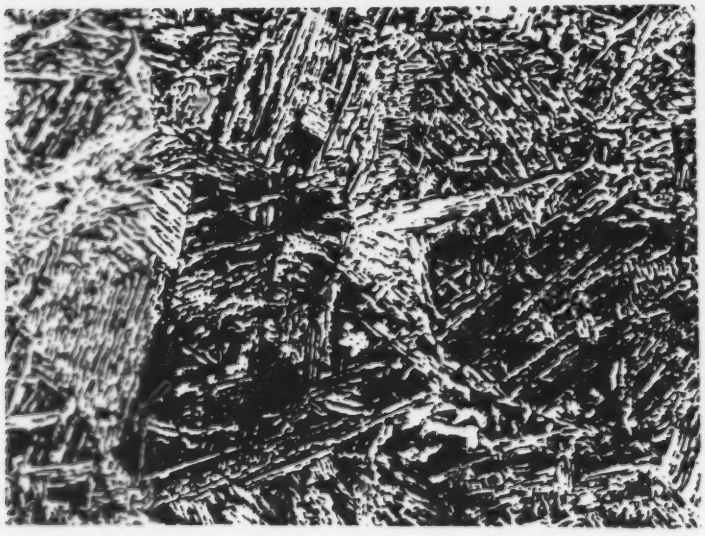

(b)

Figure 17: Steel F, Tank Test specimens, Mag x500, Etch 2% Nital
a) F21, Neg 9642 b) F31, Neg 9644

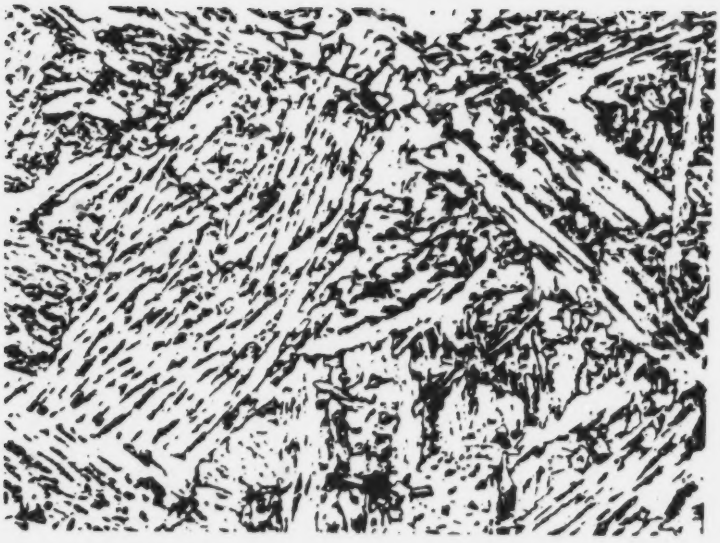

(c)

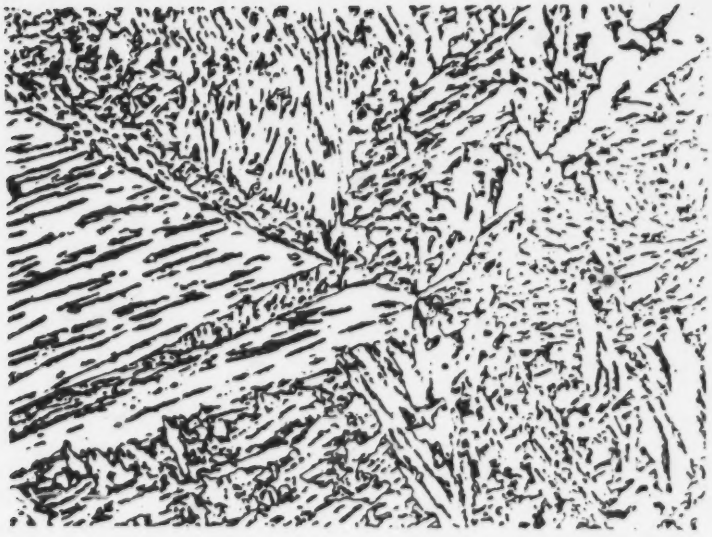

(d)

Figure 17 (continued): c) F62, Neg 9651 d) F72, Neg 9653

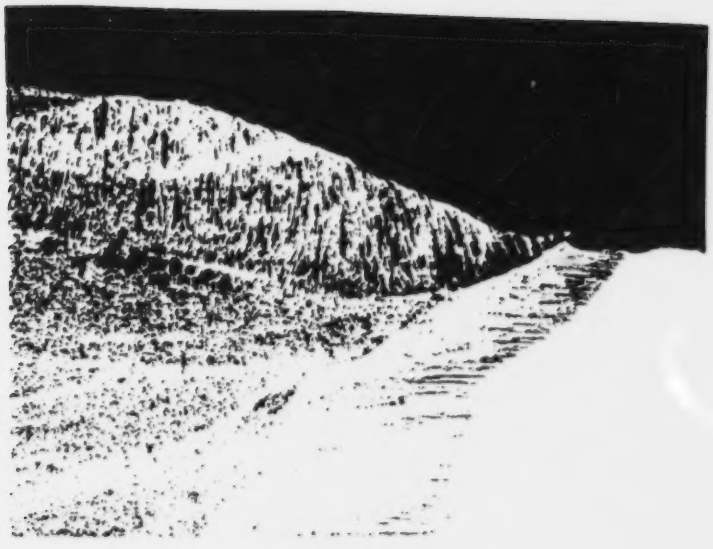

(a)

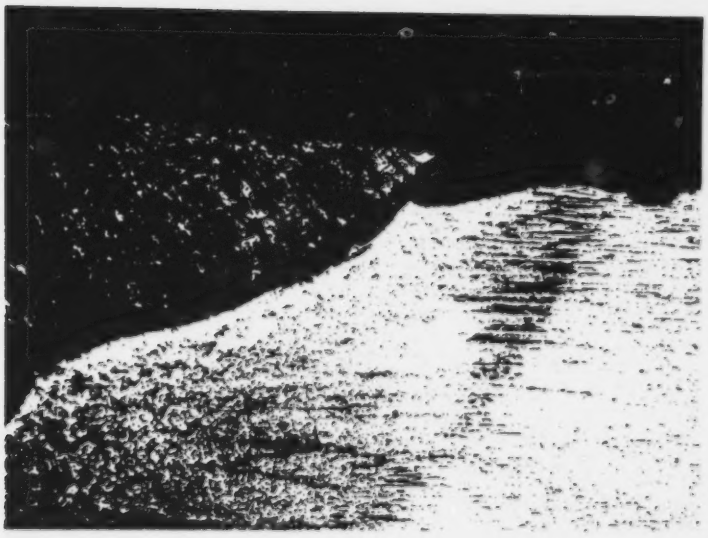

(b)

Figure 18: Steel G, Anodic Dissolution Test specimens, Mag x10, Etch 2% Nital
a) G31, Neg 9439 b) G62, Neg 9454

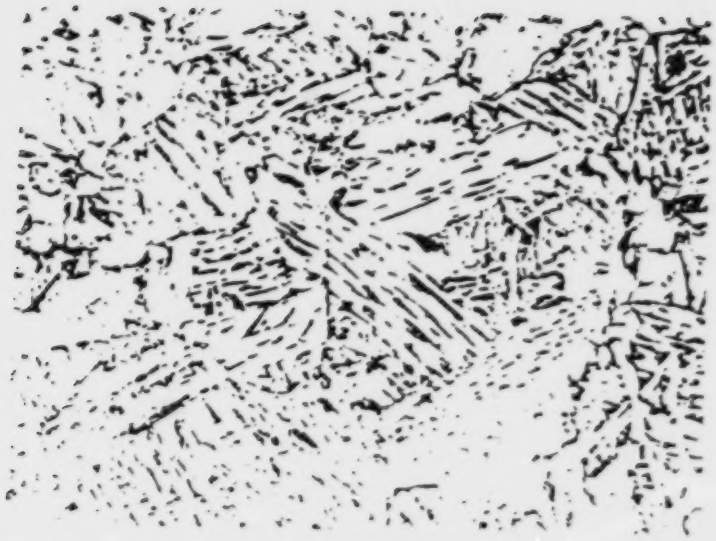

(a)

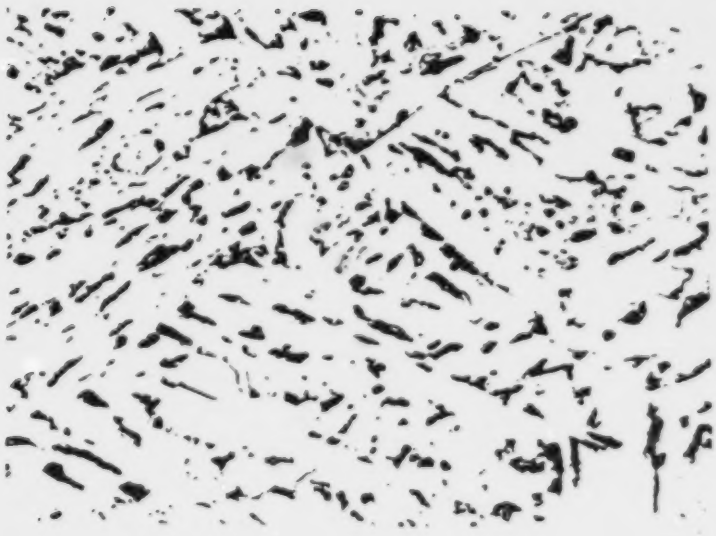

(b)

Figure 19: Steel G, Anodic Dissolution Test specimens, Mag x1000, Etch 2% Nital; a) G31, Neg 9796 b) G62, Neg 9806

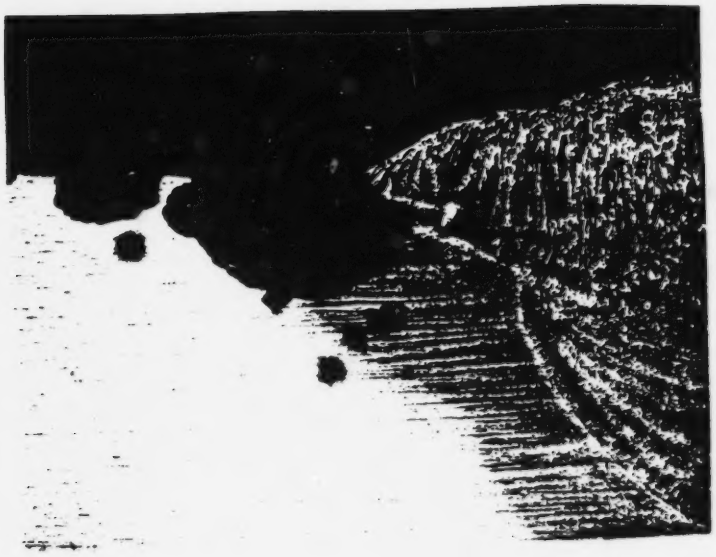

(a)

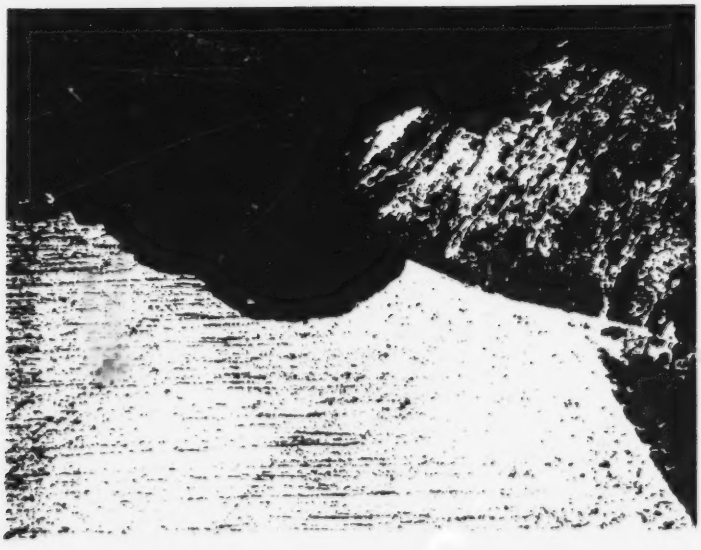

(b)

Figure 20: Steel G, Tank Test specimens, Mag x10, Etch 2% Nital
a) G31, Neg 9672 b) G62, Neg 9355

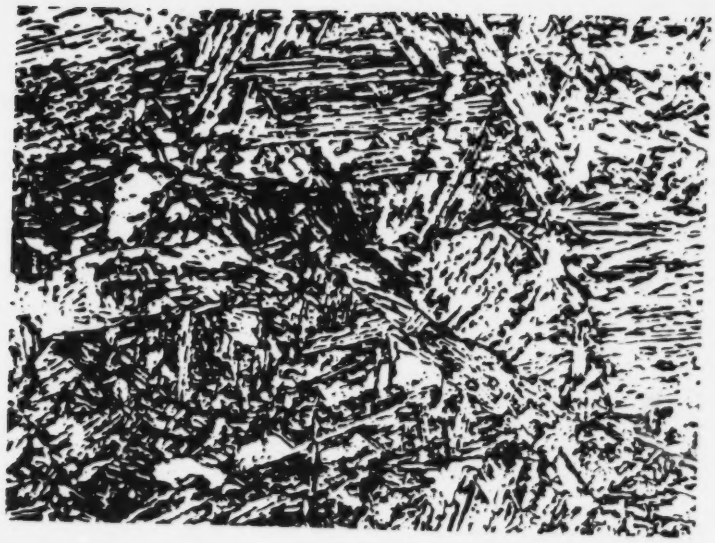

(a)

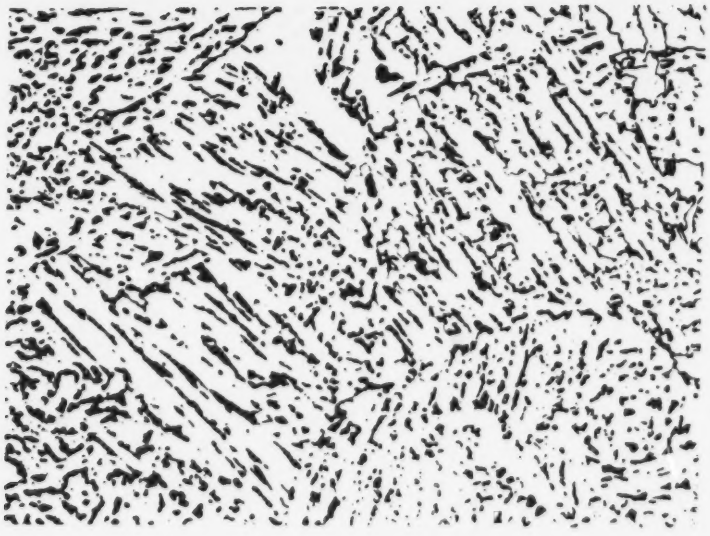

(b)

Figure 21: Steel G, Tank Test specimens, Mag x500, Etch 2% Nital
a) G31, Neg 9654 b) G62, Neg 9655

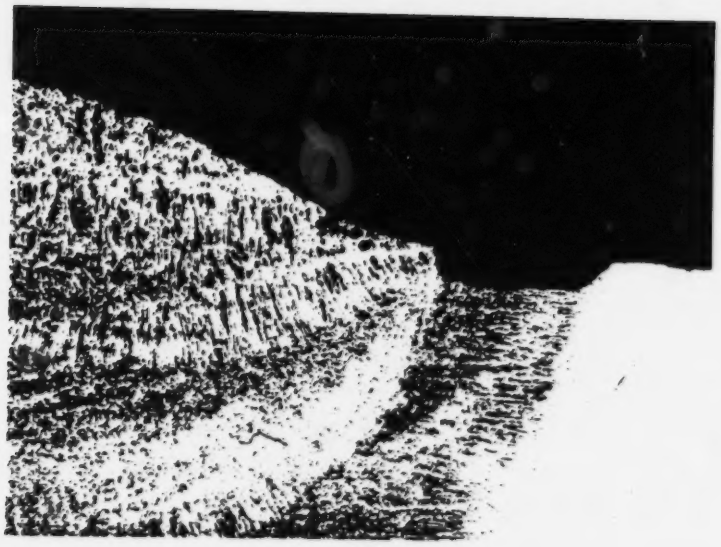

(a)

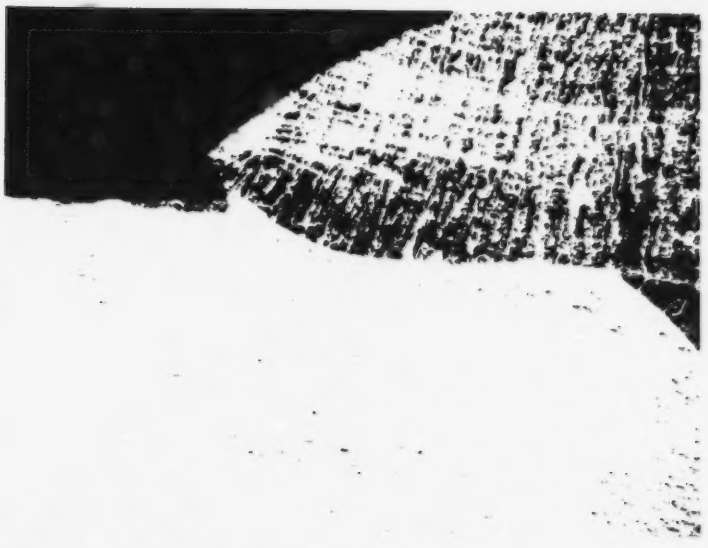

(b)

Figure 22: Steel H, Anodic Dissolution Test specimens, Mag x10, Etch 2% Nital
a) H31, Neg 9441 b) H62, Neg 9711

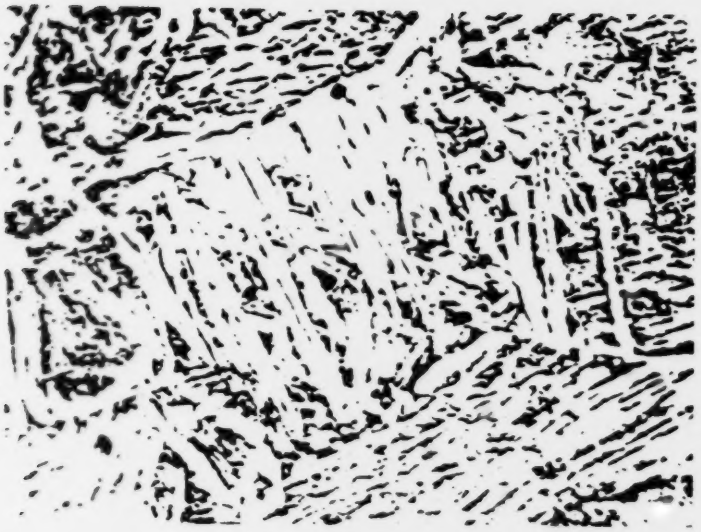

(a)

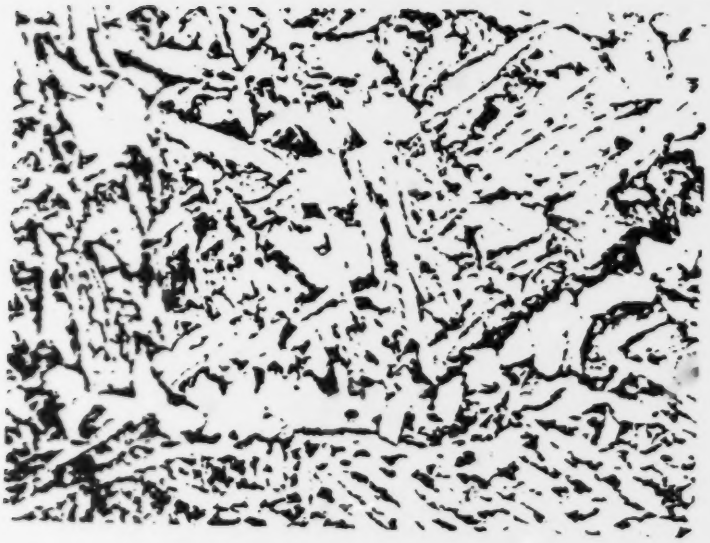

(b)

Figure 23: Steel H, Anodic Dissolution Test specimens, Mag x1000, Etch 2% Nital; a) H31, Neg 9797 b) H62, Neg 9810

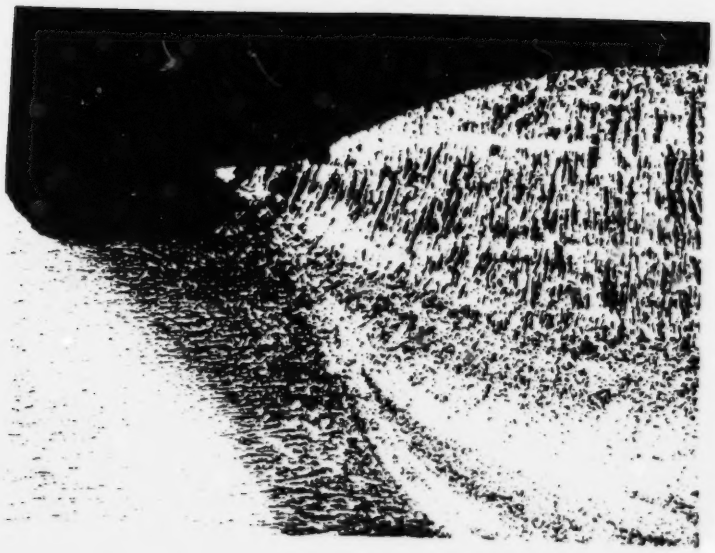

(a)

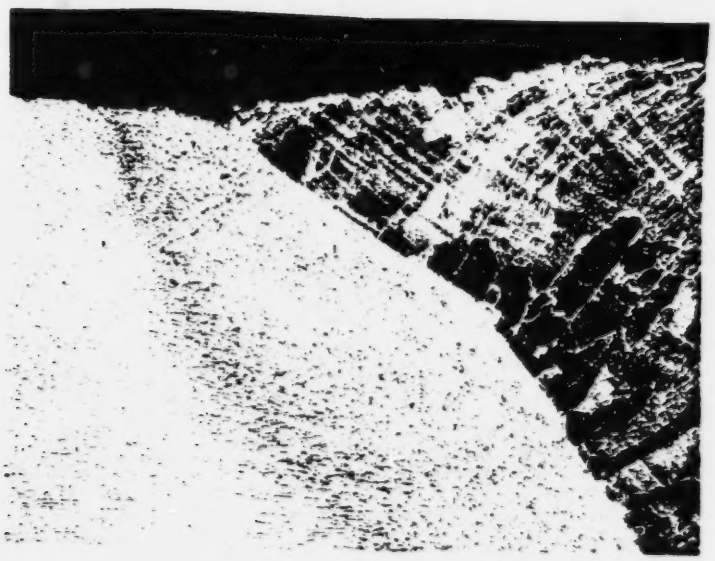

(b)

Figure 24: Steel J, Anodic Dissolution Test specimens, Mag x10, Etch 2% Nital
a) J31, Neg 9443 b) J62, Neg 9456

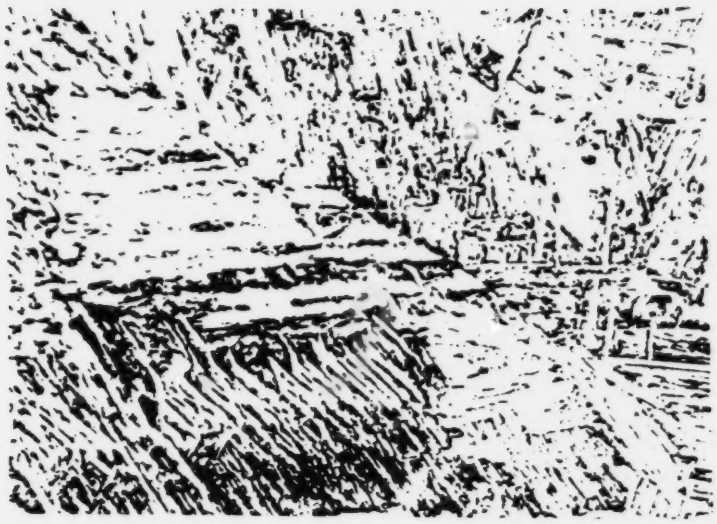

(a)

(b)

Figure 25: Steel J, Anodic Dissolution Test specimens, Mag x1000
Etch 2% Nital; a) J31, Neg 9798 b) J62, Neg 9808

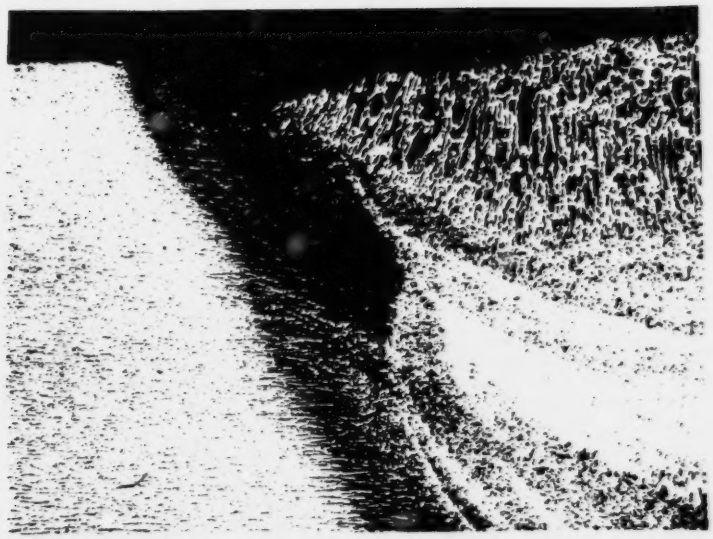

(a)

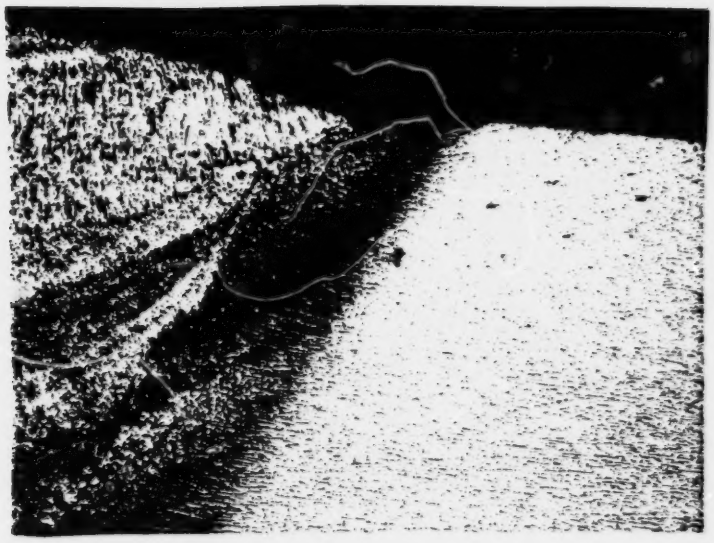

(b)

Figure 26: Steel B, Anodic Dissolution Test specimens, Mag x10, Etch 2% Nital
a) B21, Neg 9459 b) B31, Neg 9429

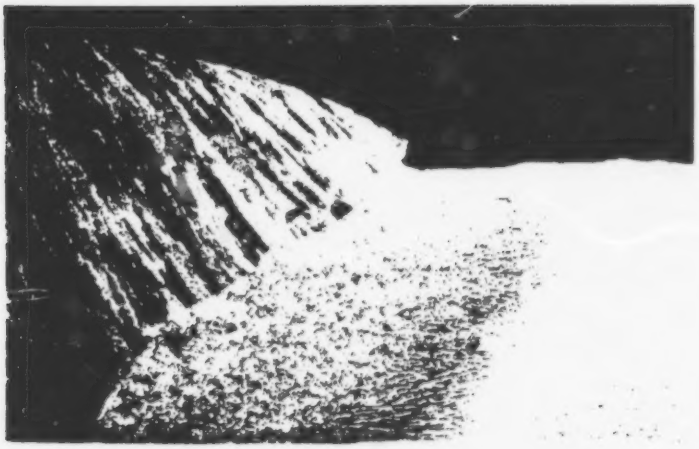

(c)

(d)

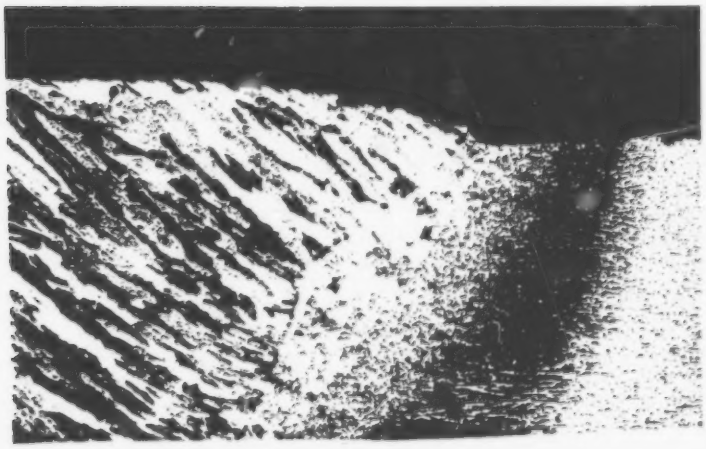

(e)

Figure 26 (continued): c) B61, Neg 9462 d) B62, Neg 9673 e) B71, Neg 9487

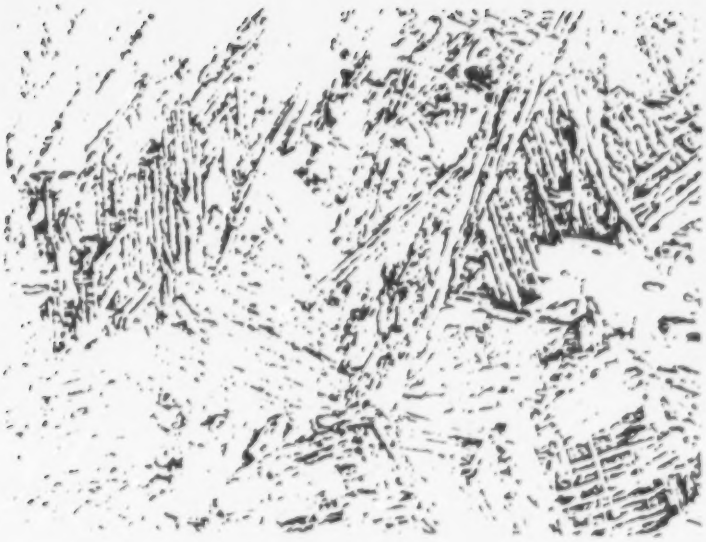

(a)

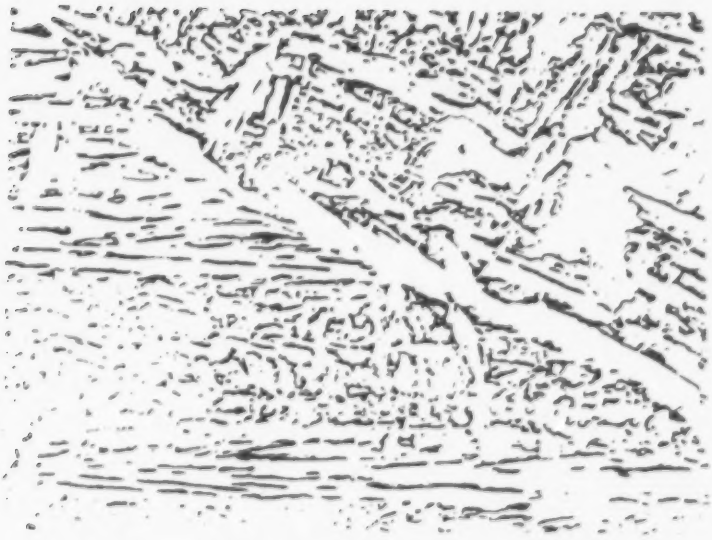

(b)

Figure 27: Steel B, Anodic Dissolution Test specimens, Mag x1000, Etch 2% Nital; a) B31, Neg 9789 b) B62, Neg 9819

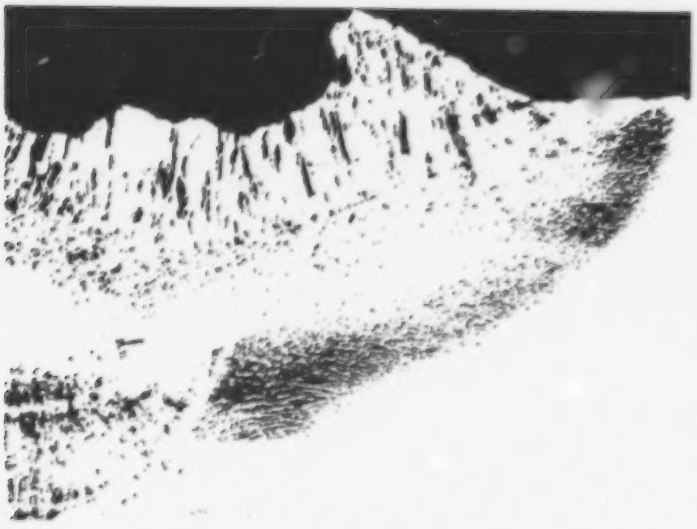

(a)

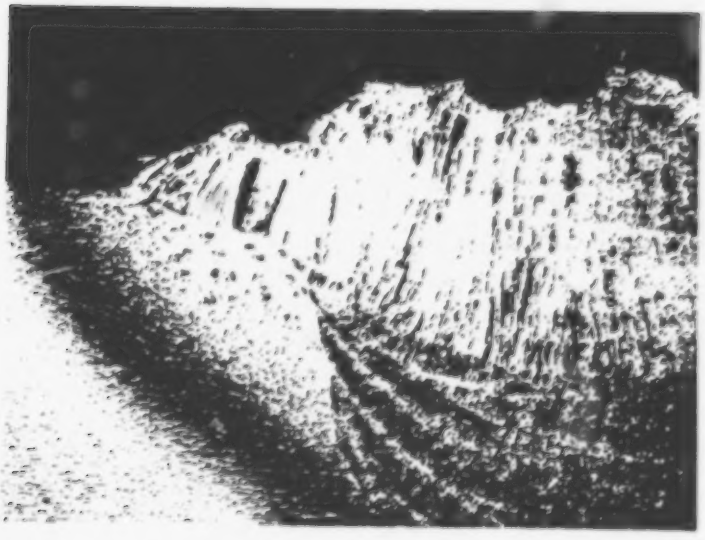

(b)

Figure 28: Steel B, Tank Test specimens, Mag x10, Etch 2% Nital
a) B21, Neg 9321 b) B31, Neg 9322

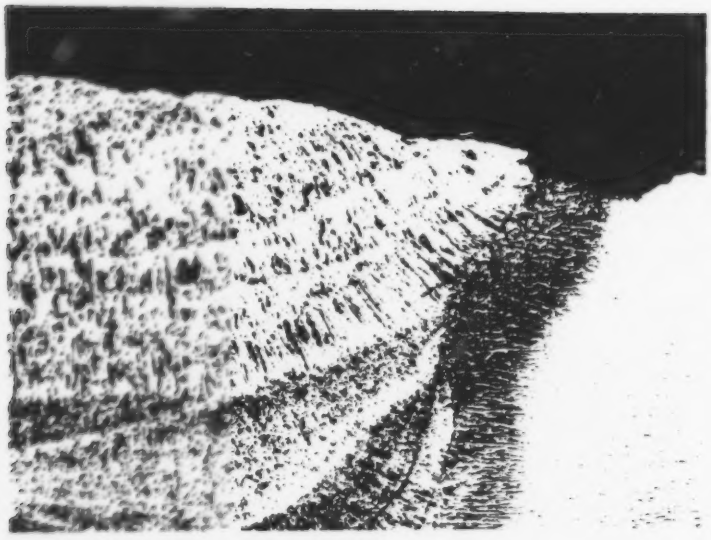

(c)

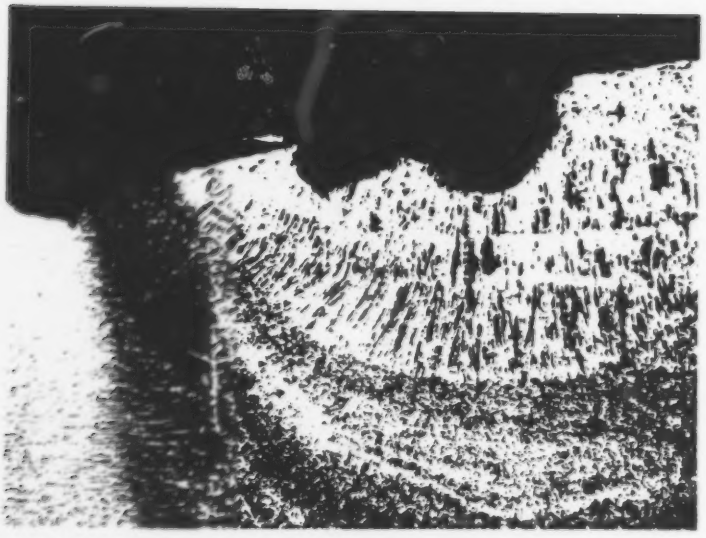

(d)

Figure 28 (continued): c) B32 (left), Neg 9325 d) B32 (right), Neg 9324

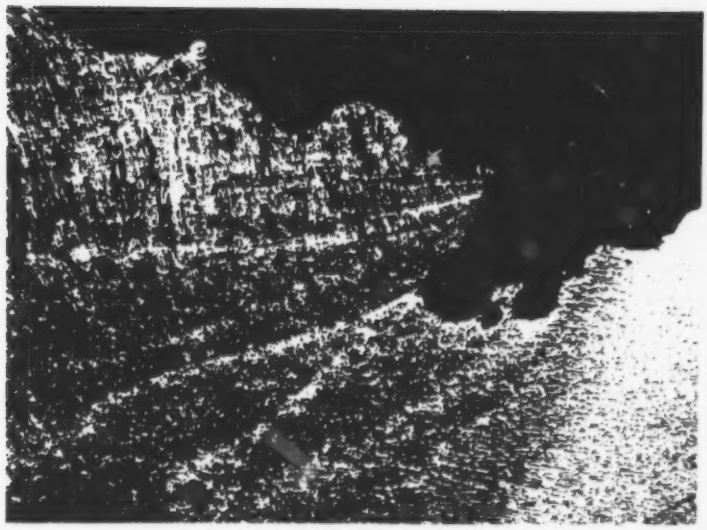

(e)

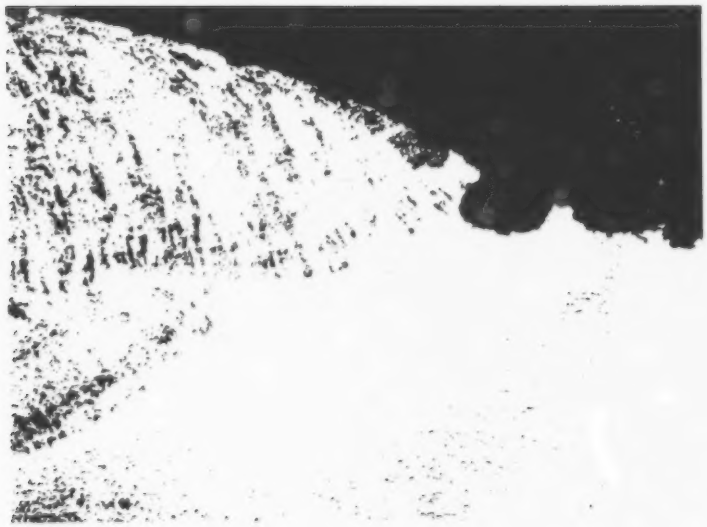

(f)

Figure 28 (continued): e) B61, Neg 9327 f) B62, Neg 9328

(g)

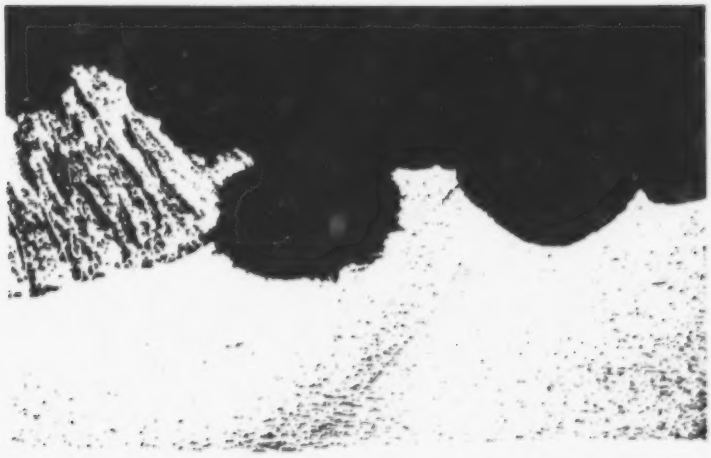

(h)

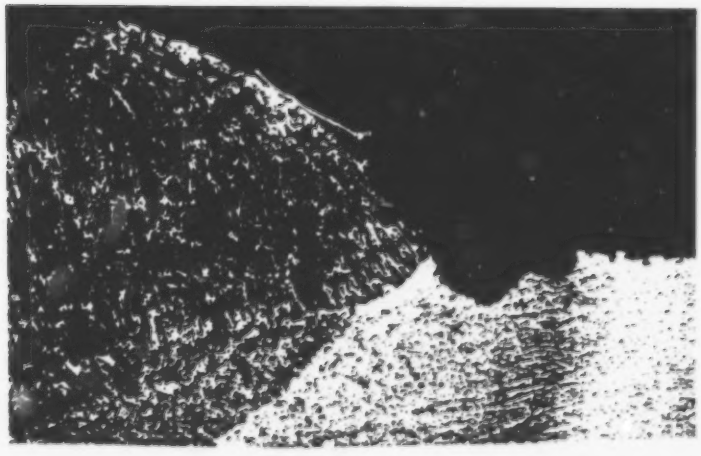

(i)

Figure 28 (continued): g) B71, Neg 9331 h) B72 (left), Neg 9333
i) B72 (right), Neg 9332

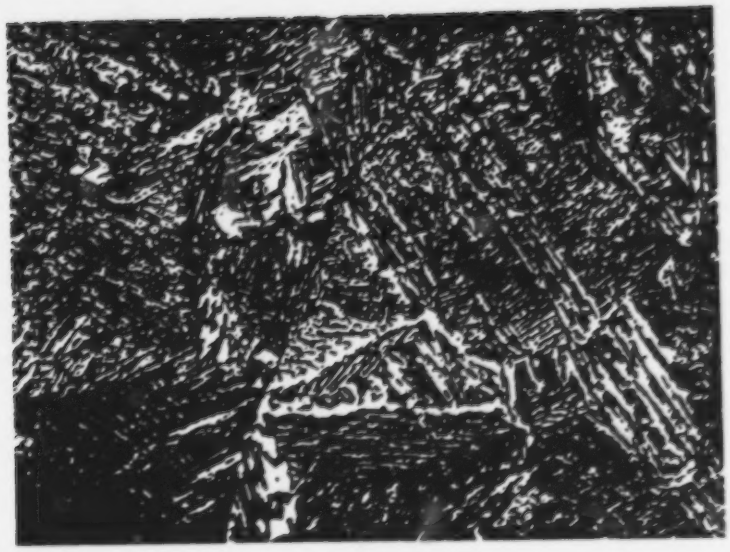

(a)

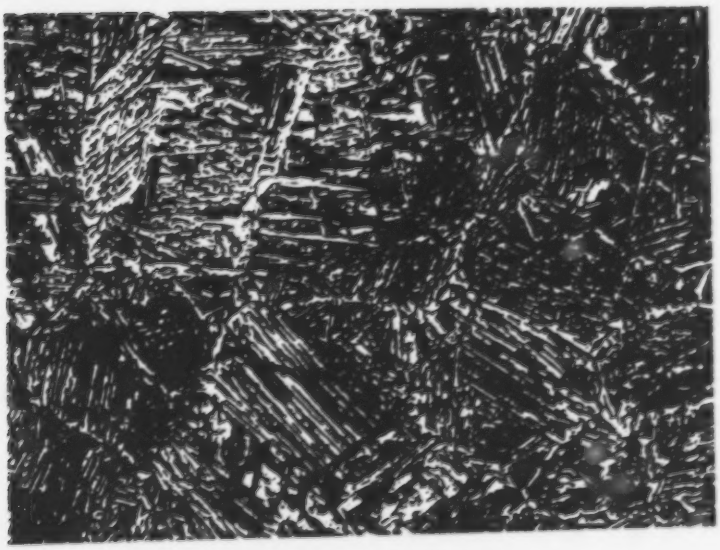

(b)

Figure 29: Steel B, Tank Test specimens, Mag x500, Etch 2% Nital
a) B21, Neg 9499 b) B31, Neg 9500

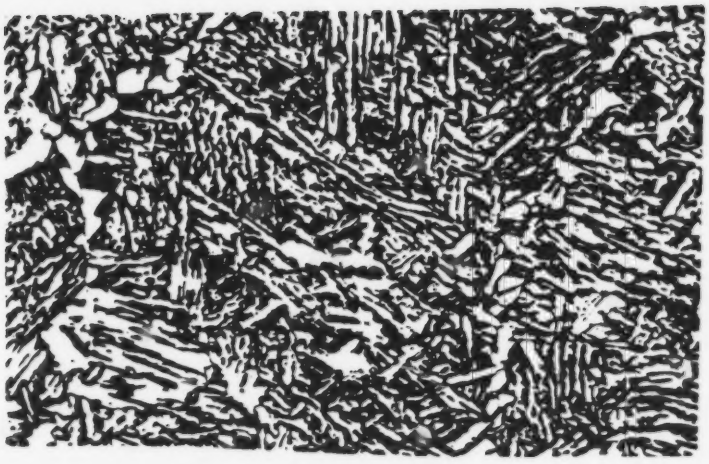

(c)

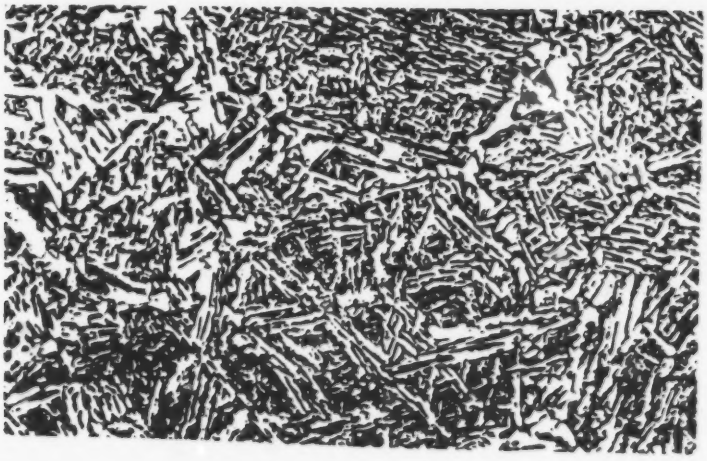

(d)

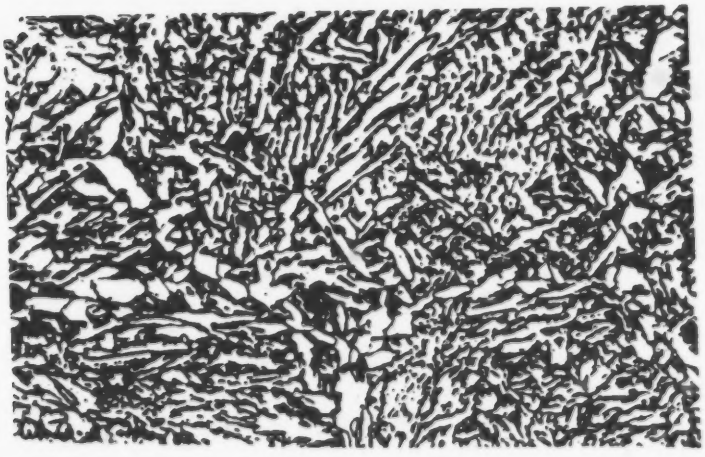

(e)

Figure 29 (continued): c) B62, Neg 9515 d) B71, Neg 9517 e) B72, Neg 9519

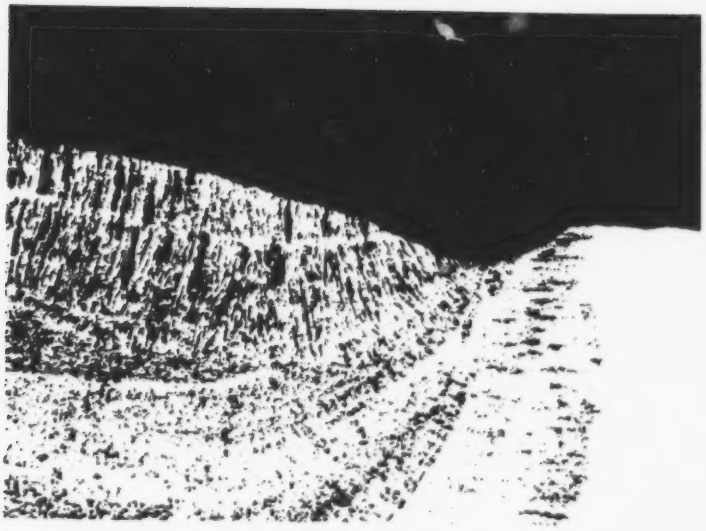

(a)

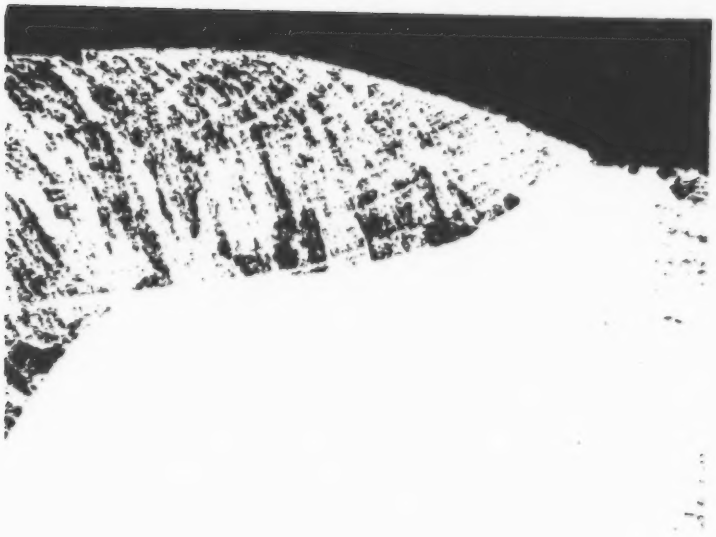

(b)

Figure 30: Steel E, Anodic Dissolution Test specimens, Mag x10, Etch 2% Nital
a) E31, Neg 9435 b) E62, Neg 9709

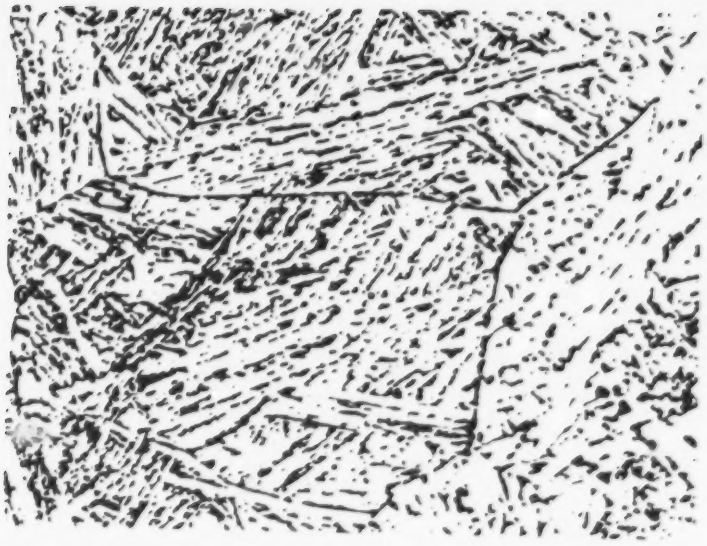

(a)

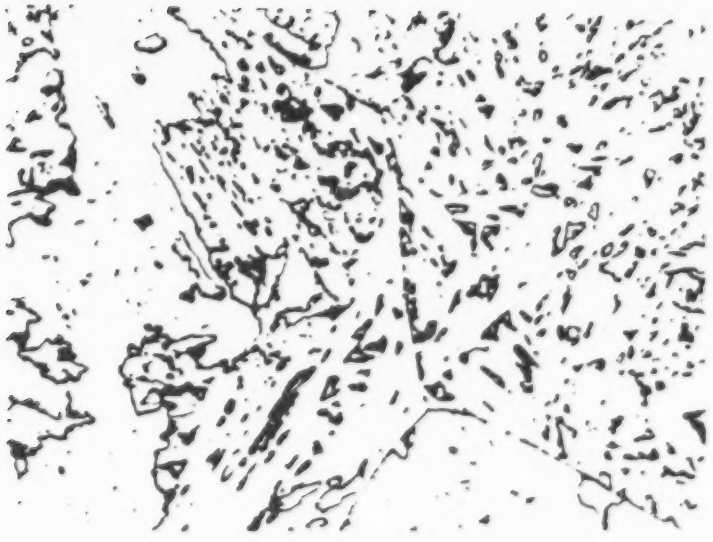

(b)

Figure 31: Steel E, Anodic Dissolution Test specimens, Mag x1000, Etch 2% Nital; a) E31, Neg 9793 b) E62, Neg 9812

(a)

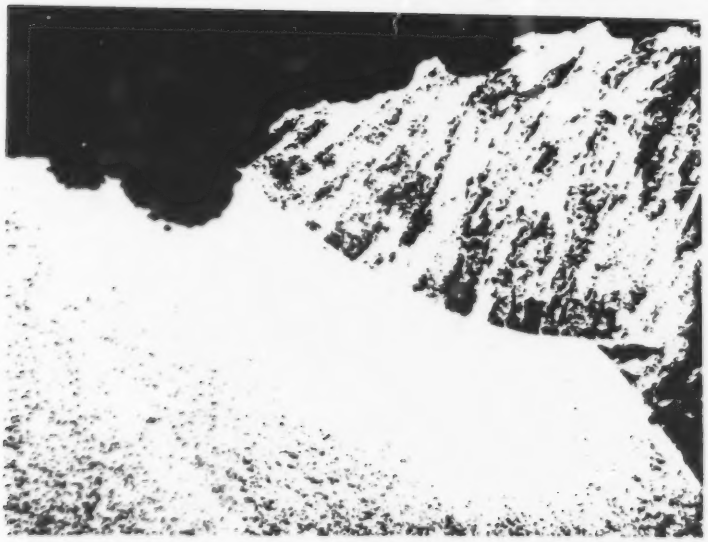

(b)

Figure 32: Steel E, Tank Test specimens, Mag x10, Etch 2% Nital
a) E31, Neg 9335 b) E62, Neg 9337

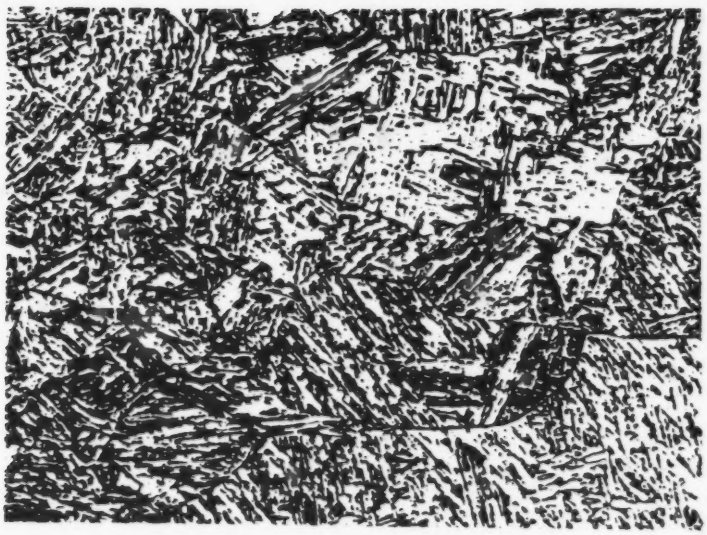

(a)

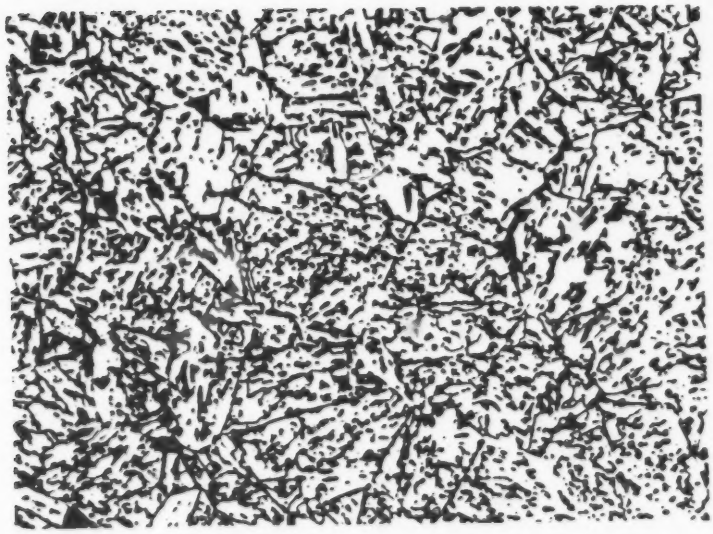

(b)

Figure 33: Steel E, Tank Test specimens, Mag x500, Etch 2% Nital
a) E31, Neg 9520 b) E62, Neg 9521

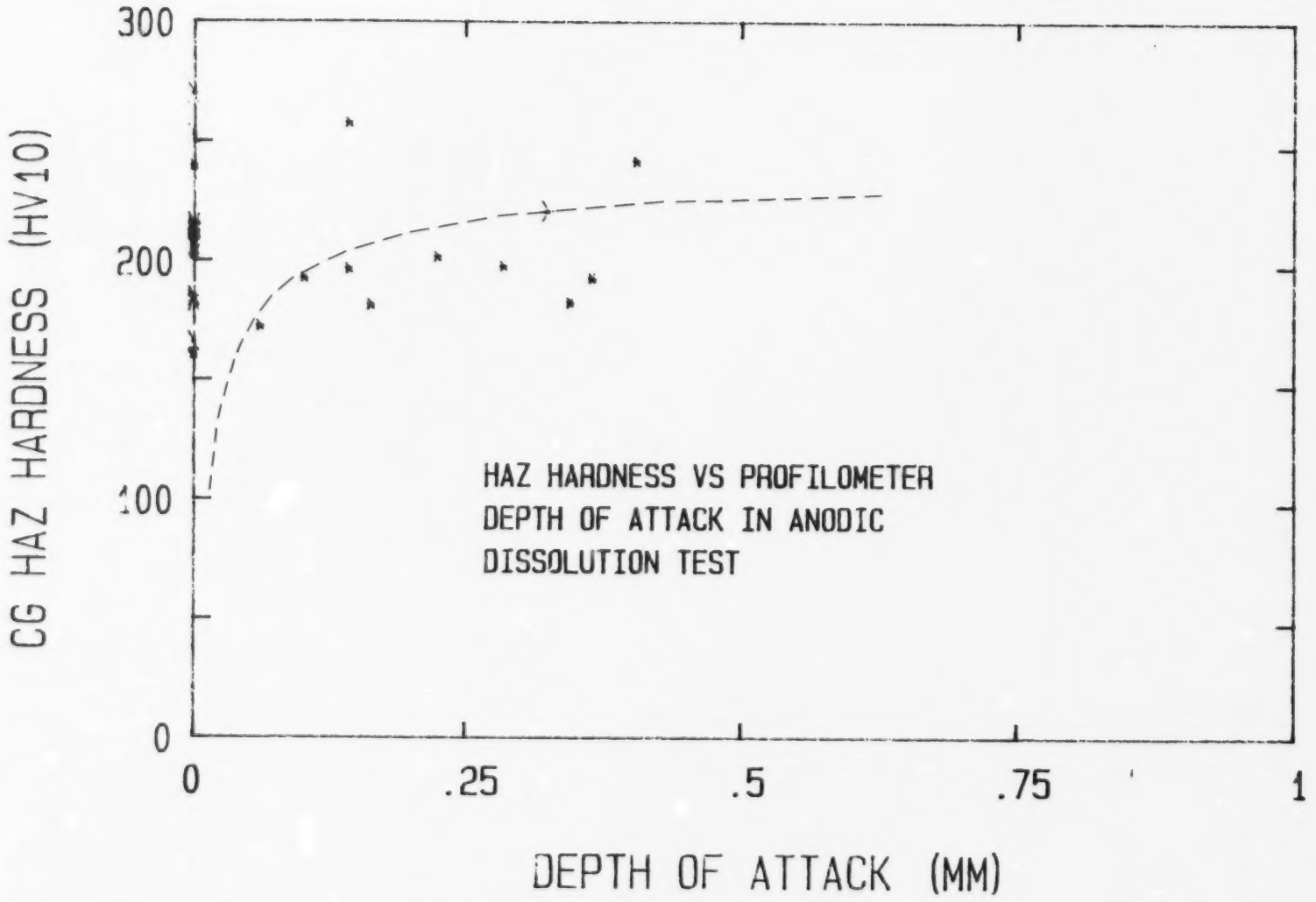

Figure 34: Effect of coarse-grain HAZ hardness on extent of HAZ corrosion in the Anodic Dissolution Test

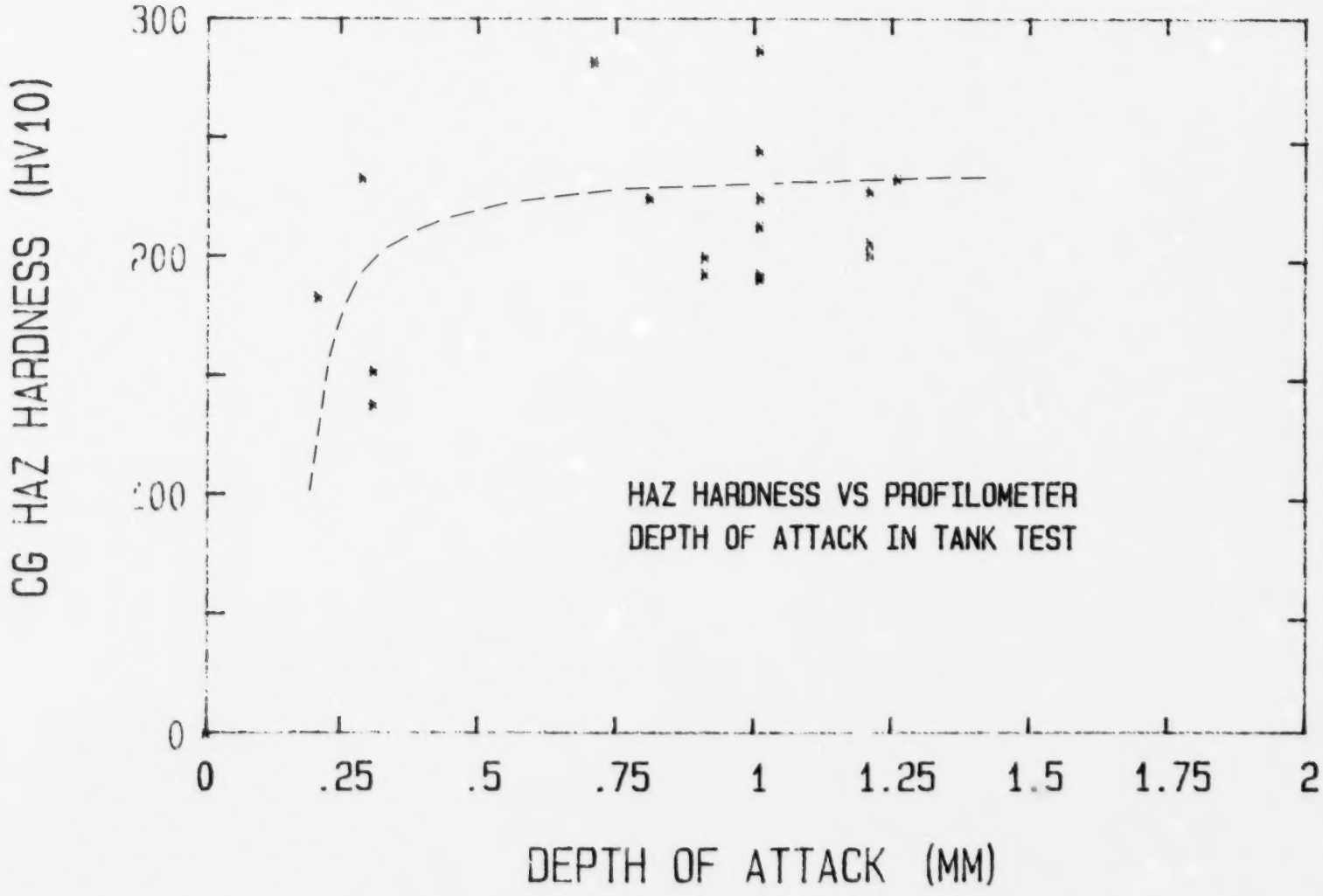

Figure 35: Effect of coarse-grain HAZ hardness on extent of HAZ corrosion in Tank Test

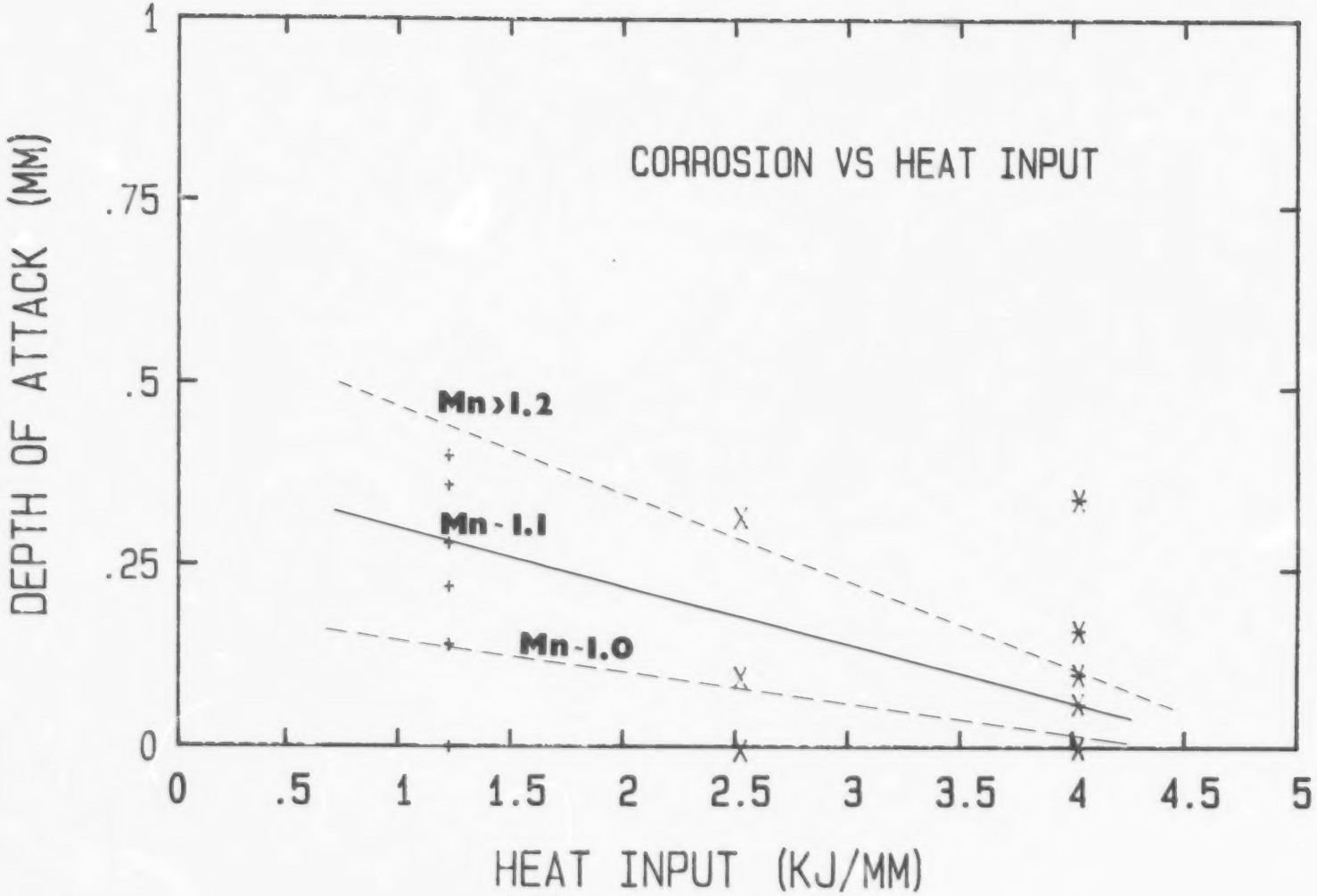

Figure 36: Effect of heat input on extent of corrosion in the Anodic Dissolution Test

APPENDIX I

PROFILOMETRY RESULTS

APPENDIX I

TABLE 1: DEPTH OF WELD METAL ATTACK - ANODIC DISSOLUTION TESTS ON BUTT WELDS

Anodic dissolution tests in stagnant 3.5% sodium chloride solutions exposed to air at room temperature. Current density - 0.88 mA/cm2.

Heat Inputs: 1) SMAW Consumables - Low (1) - 1.2 } kJ/mm
High (2) - 2.5 }

2) SAW Consumables - Low (1) - 2.5 } kJ/mm
High (2) - 4.0 }

Depths of attack expressed in μm.

Base Metal Steel	Code	SMAW								SAW							
		1		2		3		4		5		6		7		8	
		1	2	1	2	1	2	1	2	1	2	1	2	1	2	1	2
A710	E	520	460	920	860	<100			600	640	200			160			
ASTM A36	K	420	360	1110	840			260	120	430	650						
CSA G40.21 260WT	D			840	440					660	540						
CSA G40.21 350AT	B	260	240	740	300	140	40	200	180	780	300						
CSA G40.21 300W	A			460	300					720	620						
CSA G40.21 350WT	C			460	380					400	440						
Shoralsim 355Z	L			440	500					760							
Algoma LT60	F			760	780					260	300						
Stelco 350 WT	G			720	420					520							
Stelco	H			360	380					880	540						
Kawasaki EH36	J			660	400					760	780						

WELD METAL	OK73.08	7018-1	8018-C1	8018-W	L60/761	SD2-3Ni	Tibor22	Thyssen S2Ni1
Manganese	1.16	1.40	0.91	0.96	1.85	0.95	1.01	1.16
Silicon	0.37	0.37	0.31	0.38	1.12	0.27	0.17	0.22
Copper	0.35	0.04	0.03	0.19	0.07	0.09	0.17	0.04
Nickel	0.55	0.05	1.92	1.40	0.02	2.79	0.06	1.23
Molybdenum	-	-	0.01	0.03	-	0.11	0.24	-

APPENDIX I

TABLE 2: DEPTH OF HEAT AFFECTED ZONE ATTACK - ANODIC DISSOLUTION TESTS ON BUTT WELDS

Conditions as in Table I of this Appendix.

Base Metal Steel	Code	kJ/mm	SMAW								SAW							
			1.2				2.5				2.5				4.0			
		Weld:	1	2	3	4	1	2	3	4	5	6	7	8	5	6	7	8
		Mn																
A710	E	0.54							< 100			100						
ASTM A36	K	0.75			160				160			120	160	110			50	20
CSA G40.21 260WT	D	1.01	< 100		140	180	120		160	220		100	100	100		100	100	100
CSA G40.21 350AT	B	1.08										100	< 100	< 100			< 100	
CSA G40.21 300W	A	1.10	240		280	80	160		120	80		80	100	120		60	60	
CSA G40.21 350WT	C	1.24	180		360	220	200		320	340		280	160			160	140	
Shorasim 355Z	L	1.24	200		500	180			280			140	240	120				
Algoma LT60	F	1.39	360		400	180	400			400			340	500		100	300	
Stelco 350 WT	G	1.40	240		220	340	560		440	220		500	280	320		340	520	280
Stelco	H	1.40	380		480	240	100		500	400		500	260	340		180		240
Kawasaki EH36	J	1.45	500		540	500	400		560	380		320	460	380		260	240	380

Volume

2

Research & Technology Centre

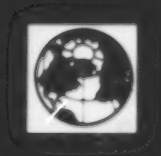

Accepted
2/16/87
with typos
noted on pg 2

[redacted]

REPORT NO: 7-186-088/Final CLASS: 4

TITLE: Metallographic Examination of
Corrosion Test Samples
(Volume 2)

DATE: February 5/87 AUTHOR: G.C. Weatherly

APPROVED: GM

TITLE: METALLOGRAPHIC EXAMINATION OF CORROSION TEST SAMPLES

FINAL REPORT

BY

S. Santyr (Volume 1)

G. Weatherly (Volume 2)

Work on this project was conducted under the auspices of the Department of Energy, Mines and Resources
This work was also supported in part by the Federal Panel on Energy Research and Development (P.E.R.D.).

DSS FILE NUMBER: 03SQ.23440-6-9110

DSS CONTRACT NUMBER: 23440-6-9110/01-SQ

EMR SCIENTIFIC AUTHORITY: Dr. R. Brigham

Introduction

Six mounted steel samples removed from the corrosion tests (described in Volume 1 of this report) were provided to the author by S. Santyr. The designations on the back of these samples were F31 FULL, F72 LEFT, K31 FULL, K72 FULL, B31 FULL and B72 LEFT. Although there was no direct information provided as to the specific welding conditions employed, it appeared that all the welds had been made by a multipass procedure, but the heat input for the "31" series was lower than that for the "72" series. All the corrosion tests had studied the HAZ region corresponding to the final weld pass i.e. a zone subjected principally to the thermal cycle associated with this final pass. This region was also delineated by a series of hardness impressions. The electron microscope observations were confined to this region in each sample, the hardness impressions proved to be convenient markers for identifying the three regions of interest in this study, viz. the CGHAZ adjacent to the fusion line, the intercritical region where the parent plate has been reheated to a temperature between A_1 and A_3 and the subcritical region.

Metallographic procedures

Two techniques were used to examine the microstructures - scanning electron microscopy on polished and etched sections and transmission electron microscopy using C-extraction replicas. For scanning electron microscopy, the samples (as provided) were repolished and etched for 2-5 mins in a 5% picric acid/ethanol solution. This procedure gave satisfactory results for steels F and K, but for steel B (containing 0.57 wt % Ni, 0.38 wt % Cr and 0.30 wt % Cu) even prolonged etching in picral did not always clearly delineate the structure for SEM examination. The technique of C-extraction replication was used only for steel F (containing V and Nb), to study precipitation in the base-plate as well as the three different locations in the HAZ noted earlier. Standard procedures using polished and lightly etched surfaces were followed for all three locations.

Results

A Steel F - base plate

The base plate microstructure of steel F is shown in Fig. 1. At low magnification (Fig. 1a), the steel has a banded ferrite-pearlite microstructure, the individual lamellae in the pearlite being clearly visible both in the S.E.M. (Fig. 1b) and T.E.M. (Fig. 1c). At higher magnification in the TEM, a distribution of carbo-nitride particles

associated with Nb and V precipitation effects could be seen. These particles fell into two distinct size groups: a coarse distribution ~ 100-500 nm in diameter and a much finer distribution, < 20 nm in diameter (see Fig.1d). X-ray analysis showed that the coarse particles contained predominantly Nb while the finer particles contained both Nb and V.

Steel F - intercritical region

Both samples examined showed similar microstructural trends in the intercritical region - only those for F31 are presented in this report. The intercritical region is seen at low magnification in Fig. 2a, with the break up of the lamellar stucture and of the "banding" apparent. The microstructure at higher magnfication showed the expected trends with the high C regions transforming to a bainitic structure containing iron carbides (Figs. 2b, 2c). At higher magnification in the C-extraction replicas, the lath or plate-like Fe_3C particles as well as the 100-500 nm Nb(C,N) and < 20 nm (Nb,V)(C,N) particles, were clearly visible (Fig. 2d). Examination of a number of areas from this region suggested that there was little or no variation in the size and density of the Nb and V-containing particles in comparison to the base-plate microstructure.

Steel F - subcritical region

The sub-critical region for sample F72 is shown in Fig. 3. Again the trends are those expected given the microstructure of the base steel. Some spheroidization and break-up of the lamellar carbide structure is visible (Figs. 3a, 3b), but the distribution of carbo-nitride particles is identical to that in the base plate (Fig. 3c).

Steel F - C.G.H.A.Z. (F31)

The C.G.H.A.Z. adjacent to the fusion line in sample F31 is shown in Fig. 4a (at low magnification) in the S.E.M. The microstructure consists of a small amount of proeutectoid ferrite (at the prior austenite grain boundaries) and bainite. The C-rich phase at the bainite lath boundaries is mainly Fe_3C (Fig. 4b). The fusion line boundary could also be readily identified in the C extraction replica. The weld metal (Fig. 4c) contains (Mn, Si)-rich oxide inclusions and an equiaxed fine grained ferrite, while the adjacent grid on the C replica has a readily identifiable bainite

structure (Fig. 4d). Having marked the fusion line bouhdary in this way, it is then a straightforward procedure to study both the transformation microstructure and distribution of (Nb,V) rich carbo-nitrides as a function of distance from the fusion line. Figs. 4e and 4f were taken at a distance of 1.4 mms from the fusion line. The structure seen in Fig. 4e is still characteristic of an **upper bainite** with rows of Fe-rich carbides marking the interlath boundaries. At this distance from the fusion line both coarse and fine Nb(C,N) and (Nb, V)(C,N) particles are visible (Fig. 4f). The density of these coarse and fine particles as observed on the C-extraction replica diminished as the fusion line was approached. No fine particles were observed at approximately 0.7-0.8 mm distance from the fusion line and only a few coarse Nb-rich particles were found in this region. An example is given in Fig. 4g of two Nb-rich particles located approximately 150 µm from the fusion line. No Nb-rich particles were observed in the HAZ first grid region (~ 100 µm) adjacent to the fusion line. Although the maximum temperatures reached in this region of C.G.H.A.Z. are well in excess of the solubility temperature for (Nb, V)(C, N), the dissolution behaviour of the particles (time to dissolution depending on the (particle size)^2) prevents complete dissolution of the coarser particles during the thermal cycle. However, it is clear that in a region approximately 0.7 mm wide adjacent to the fusion line much/fg/the Nb and all of the V has gone into solution and has not been reprecipitated on cooling.

Steel F - C.G.H.A.Z. region (F72)

The structures and trends noted above were similar to those of F31. The coarse-grained heat affected zone is seen in the S.E.M. micrographs Fig. 5(a) - low magnification and Fig. 5(b) - high magnification. The lath size in the **bainite structure** is somewhat coarser (cf Figs 4 (a) and 5(a)), a reflection of the slower cooling rate accompanying the higher heat input of this series of welds. The interlath phase is again predominantly Fe-rich carbides (Fig. 5b).

B. Steel K - base plate, sub-critical and intercritical regions

For this steel, only scanning electron microscopy was used to follow the microstructural changes as the base plate chemistry precluded any precipitation effects of interest. Steel K is a plain C steel (0.2 wt % C) and the base plate microstructure is a relatively coarse-grained ferrite-pearlite mixture (Fig. 6a, 6b). The sub-critical region i.e. heated to

just at or below the A_1 temperature during the weld thermal cycle shows some evidence of pearlite degeneration but otherwise the microstructure is very similar to that of the base plate (cf Fig. 6a and Fig. 6c).

The intercritical region is shown in the microstructures of Fig. 7. At low magnification, Fig. 7a, the boundary between the sub-critical and intercritical regions is marked by the hardness impression. To the right of the impression the structure shows the same features as that seen in Fig. 6c i.e. degeneration of the pearlite (Fig. 7b). To the left of the impression, i.e. in the intercritical region, the structure is a mixture of equiaxed and acicular ferrite grains interspersed with areas of fine pearlite produced by cooling from above the A_1 temperature (Fig. 7c).

Steel K - C.G.H.A.Z.

At the lower heat input level (sample K31) the heat affected zone region adjacent to the fusion line contained regions of proeutectoid ferrite (at prior austenite grain boundaries), Widmanstatten ferrite with aligned carbides and fine pearlite (Fig. 8a). At the higher heat input (sample K72), the proportion of proeutectoid ferrite and Widmanstatten ferrite was greater than that in sample K31 (Fig. 8b). The fine pearlite structure could be readily resolved at higher magnification (Fig. 8c).

C. Steel B - base plate, sub-critical and intercritical regions

For this steel, scanning electron microscopy was again the only technique used to follow the microstructural changes. The base plate microstructure, shown in Figs 9a, 9b, contains a mixture of ferrite and pearlite. As we have noted earlier this sample proved to be more difficult to etch than either steels F or K, and it was particularly difficult to resolve the pearlite structure (see Fig. 9b). The sub-critical region (Fig. 9c) appears to have an identical microstructure to the base plate; the microstructural break-up of the pearlite is not readily visible in the micrograph.

The intercritical microstructure for this steel is seen at low magnification in Fig.10a. The intercritical region is shown in Fig.10b at the same magnification as Fig.9a to provide a direct comparison with the base plate microstructure. Some refinement of the structure is apparent. At higher magnification (Fig.10c) break-up of the pearlite is visible, in these regions the C-rich structure has decomposed to form bainite on cooling.

Steel B - C.G.H.A.Z.

For sample B31 (the lower heat input) the microstructure in the coarse-grained heat affected zone is a fully bainitic one. At low magnification, little or no proeutectoid ferrite is visible at the prior austenite grain boundaries (Fig.11a). At higher magnification the fine lath structure of bainite is clearly seen (Fig.11b); at this magnification no carbides or MA phase are visible and the structure is characteristic of a **lower bainite**.

For the higher heat input (sample B72), the prior austenite boundaries are decorated by pro-eutectoid ferrite (Fig. 11c) and the intragrannular structure is **upper bainite** with well defined arrays of carbides lying at the bainite lath boundaries (Fig. 11d).

The microstructures described above for this steel show the influence of the alloying elements (Cr, Ni, Cu) in giving the steel a higher hardenability so that at the lower heat input (faster cooling rate), this steel has a finer bainitic structure (with no proeutectoid ferrite) than the other 2 steels.

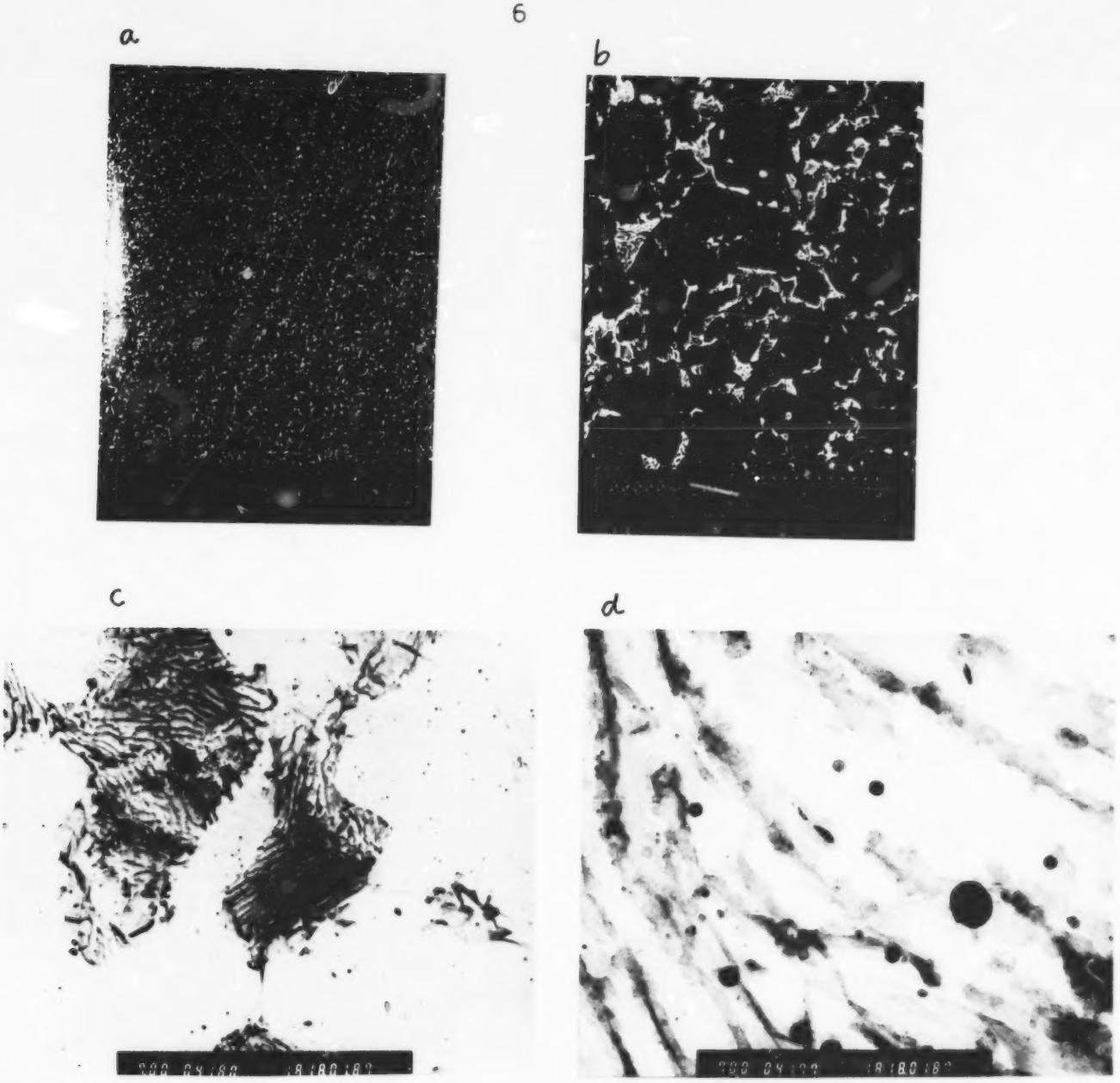

Fig.1 Microstructure of Base Plate F (a) SEM showing banded ferrite-pearlite microstructure (x300); (b) as (a) (x1000); (c) TEM of C extraction replica showing pearlite colonies and distribution of Nb rich carbides (x7000); (d) as (c), showing coarse and fine carbo-nitride particles (x70,000)

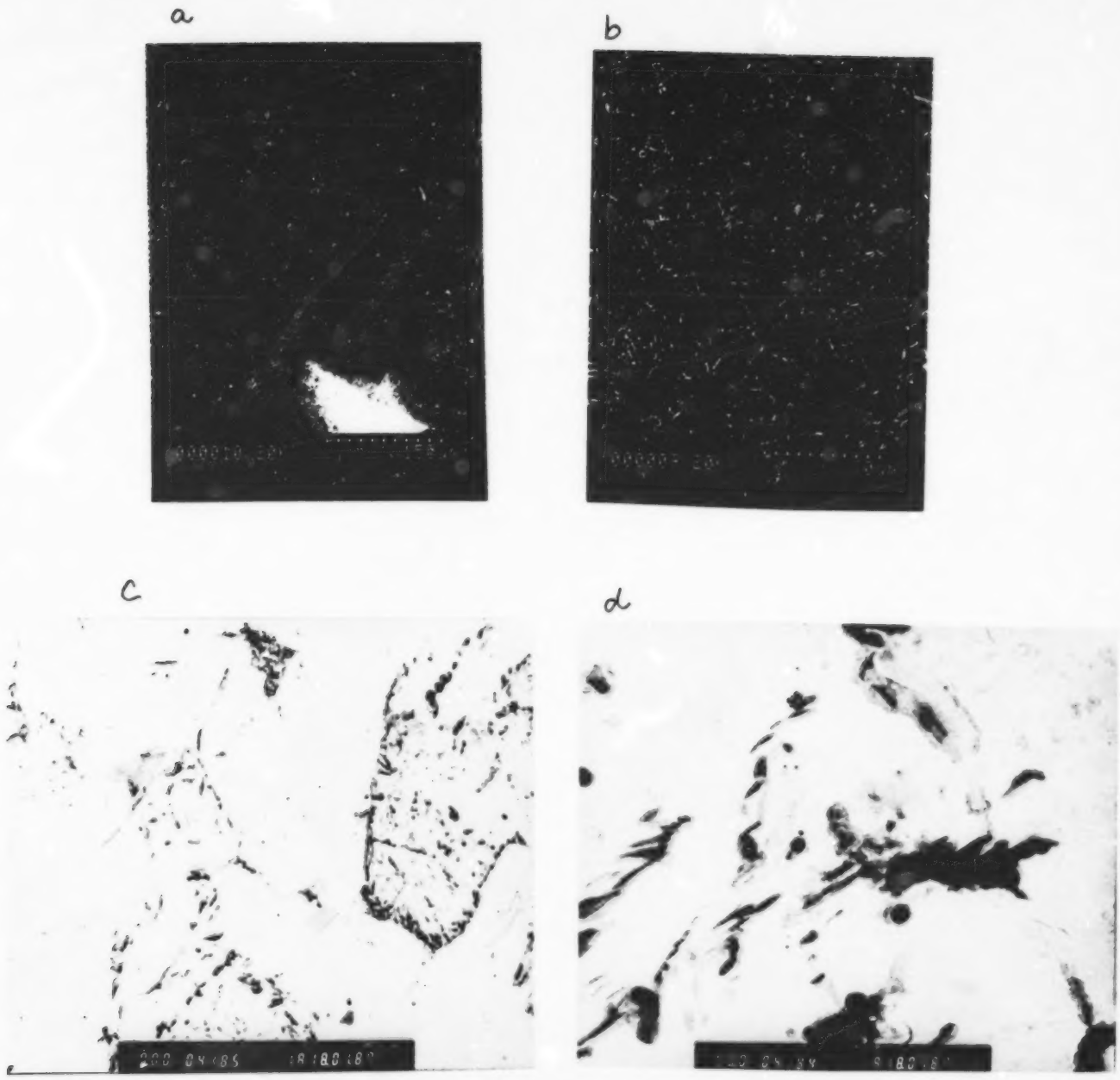

Fig. 2 (a) S.E.M. of intercritical region of HAZ of sample F31 (x200); (b) as (a) showing bainitic structure in high C regions and ferrite grains (x1000); (c) TEM of extraction replica of same area showing carbides (x7000); (d) as (c) showing Fe_3C and (Nb, V) carbo-nitrides (x50,000)

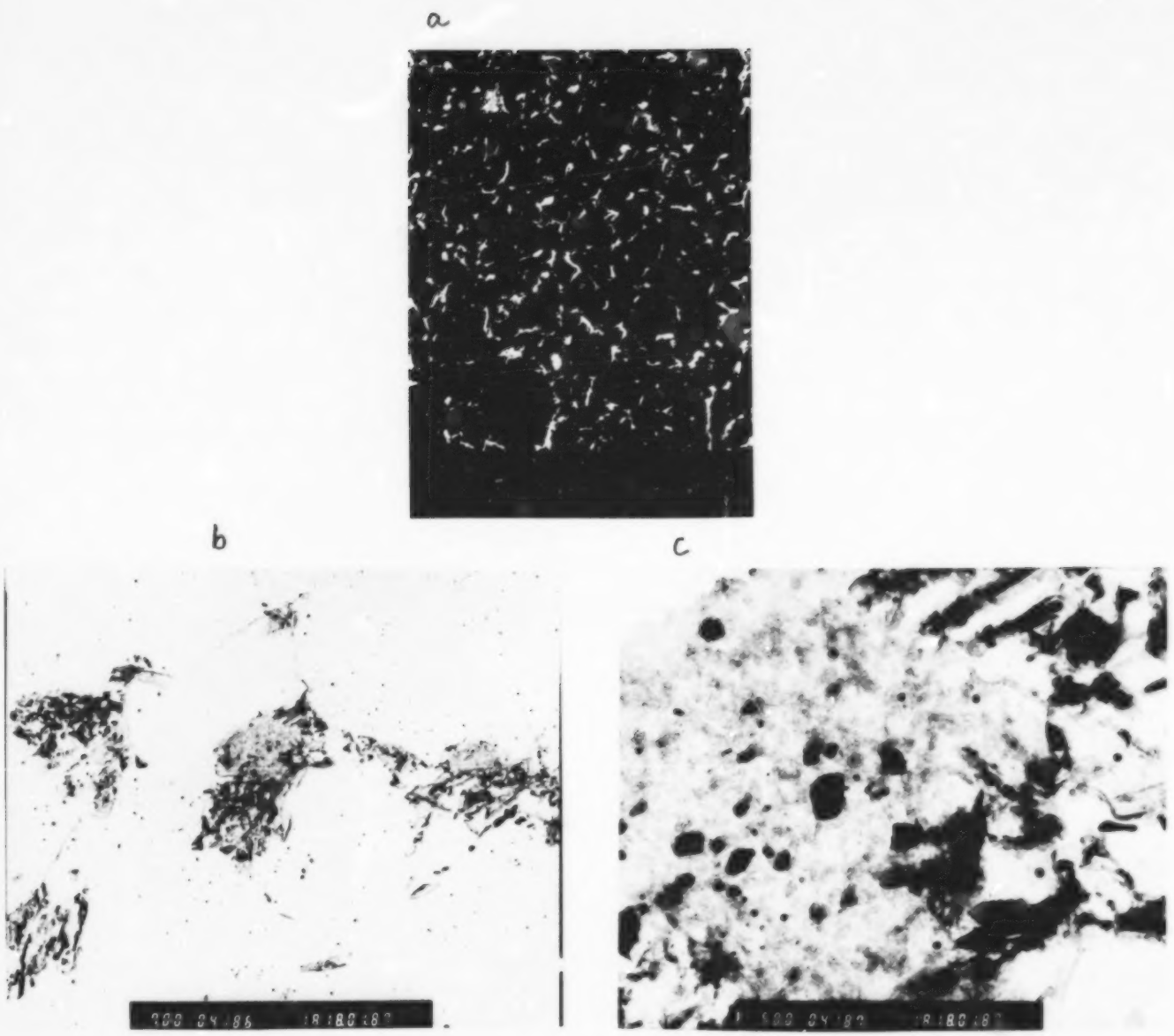

Fig. 3 Sub-critical region of sample F72 (a) S.E.M. showing spheroidization of lamellar carbides in pearlite (x1000); (b) T.E.M. of same area from carbon-extraction replica (x7000); (c) as (b) showing Fe_3C and (Nb,V) rich carbo-nitrides (x50,000)

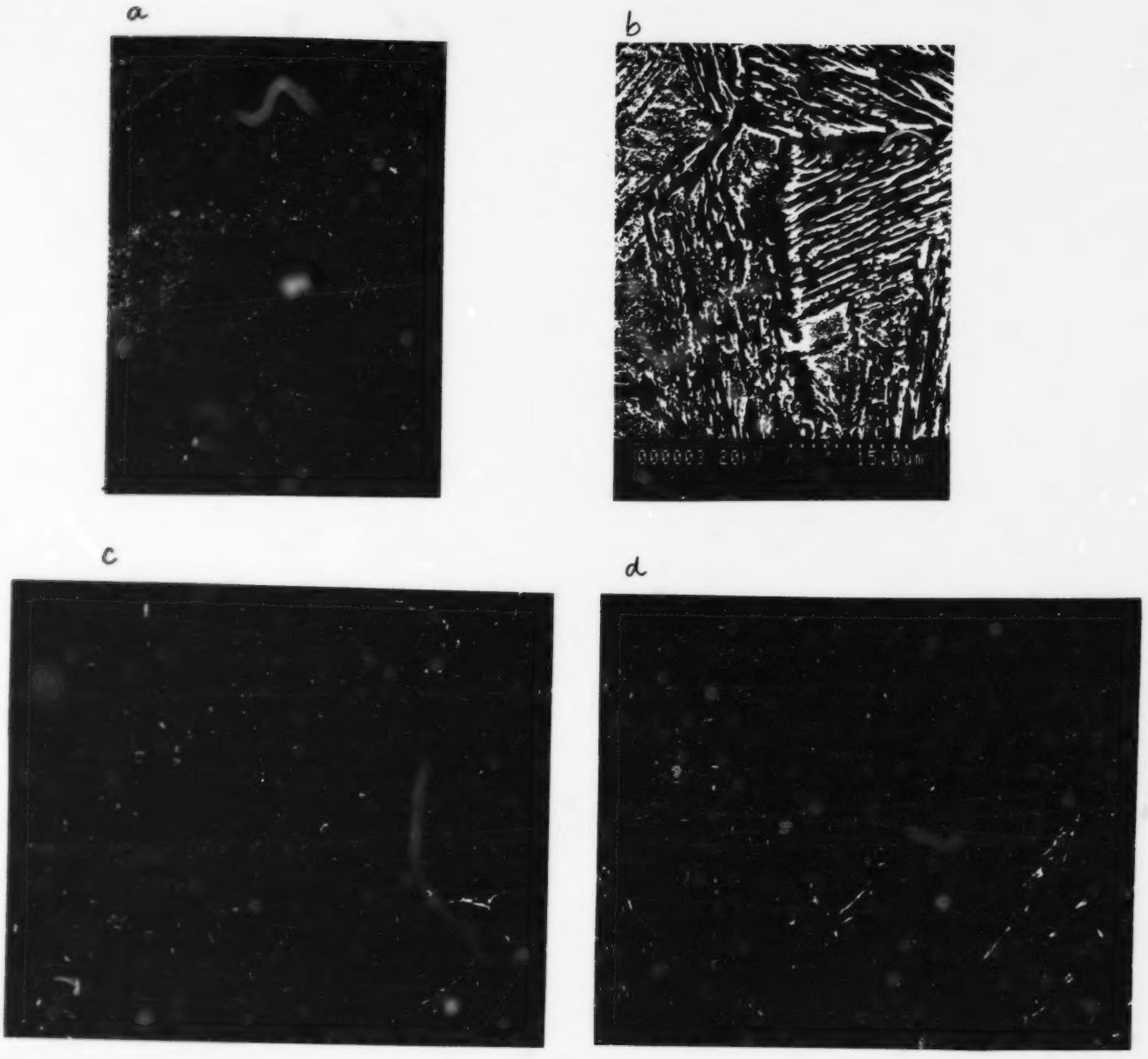

Fig. 4 Coarse-grained heat affected zone region of sample F31 (a) S.E.M. showing proeutectoid ferrite at prior austenite boundaries and bainite (x300); (b) as (a) at higher magnification showing carbides at bainite lath boundaries (x2000); (c) TEM weld metal adjacent to fusion line in C-extraction replica (x6000); (d) as (c) showing heat affected zone structure at fusion line (x6000)

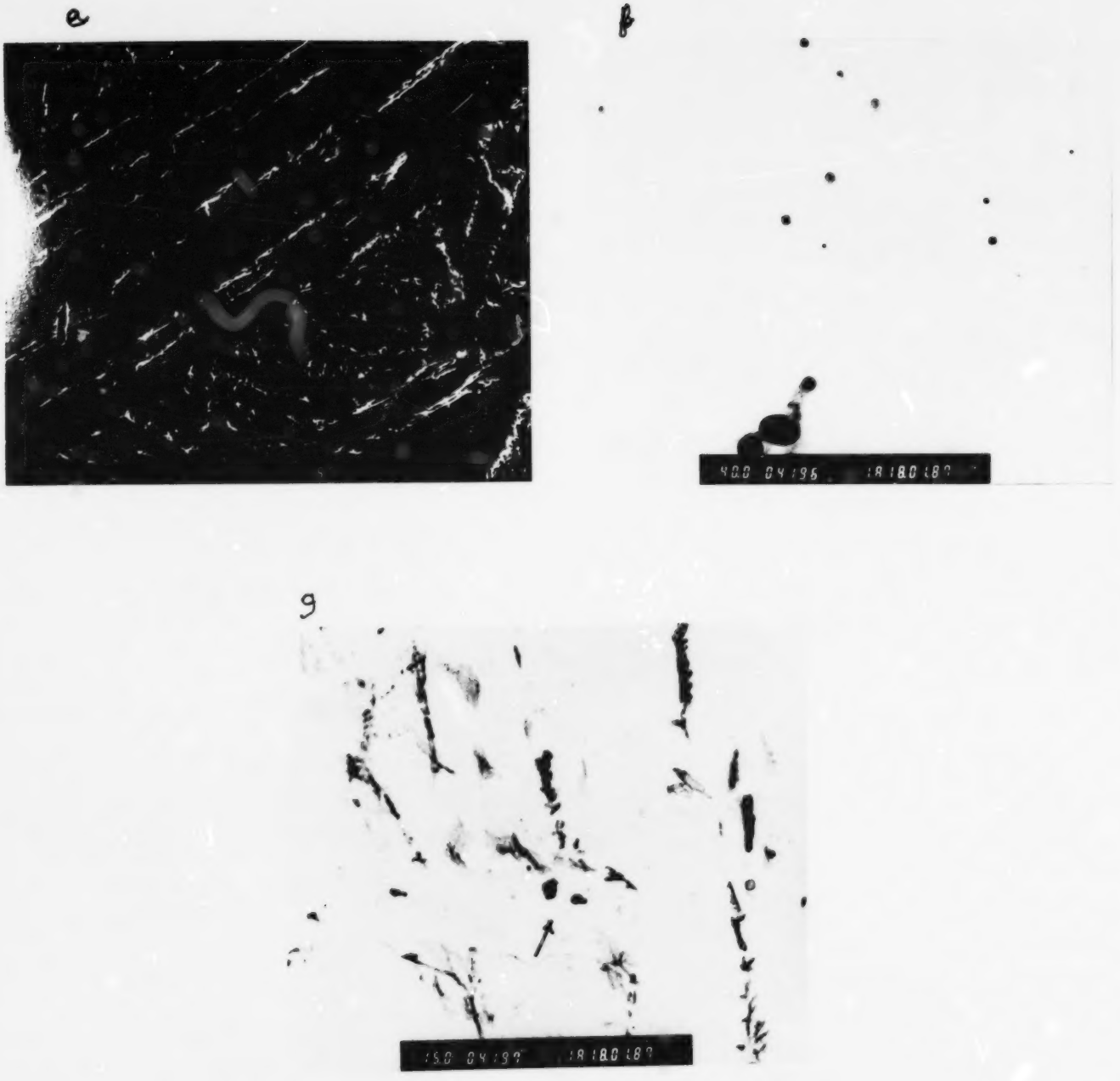

Fig. 4 (continued) (e) HAZ region 1.4 mm from the fusion line, TEM showing bainitic structure (x6000); (f) as (e), higher magnification, showing distribution of coarse and fine (Nb,V) carbo-nitrides (x40,000); (g) undissolved Nb-rich carbo-nitrides, ~ 150 µm from the fusion line (x15,000)

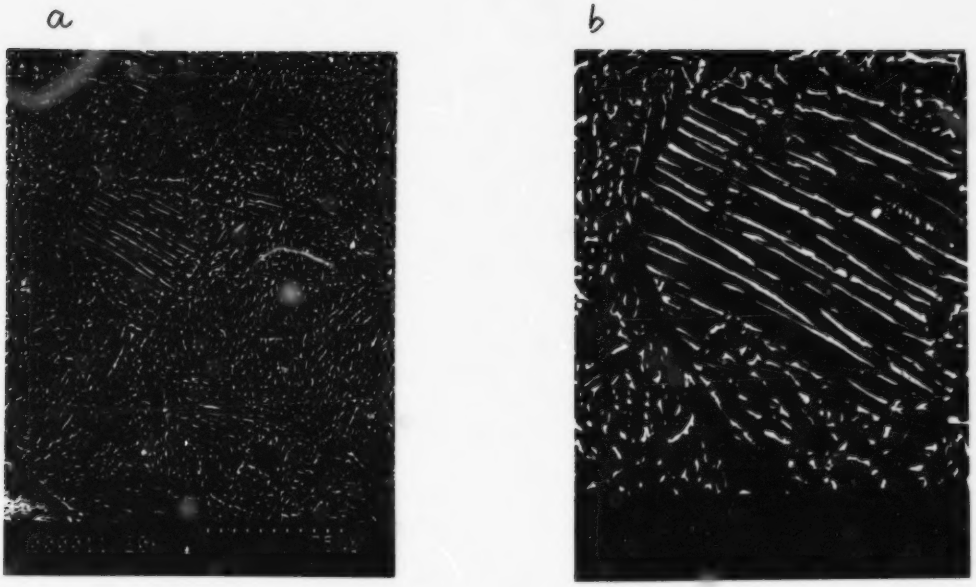

Fig. 5 Coarse-grained heat affected zone region of sample F72 (a) S.E.M. showing proeutectoid ferrite at prior austenite grain boundaries and coarse upper bainite (x400); (b) as (a) showing Fe_3C at bainite interlath boundaries (x1,200)

Fig. 6 (a) Microstructure of base plate K showing a mixed coarse grained ferrite-pearlite structure (x300); (b) as (a) (x1000); (c) sub-critical region of HAZ of sample K72 showing some break-up of the pearlite (x1000)

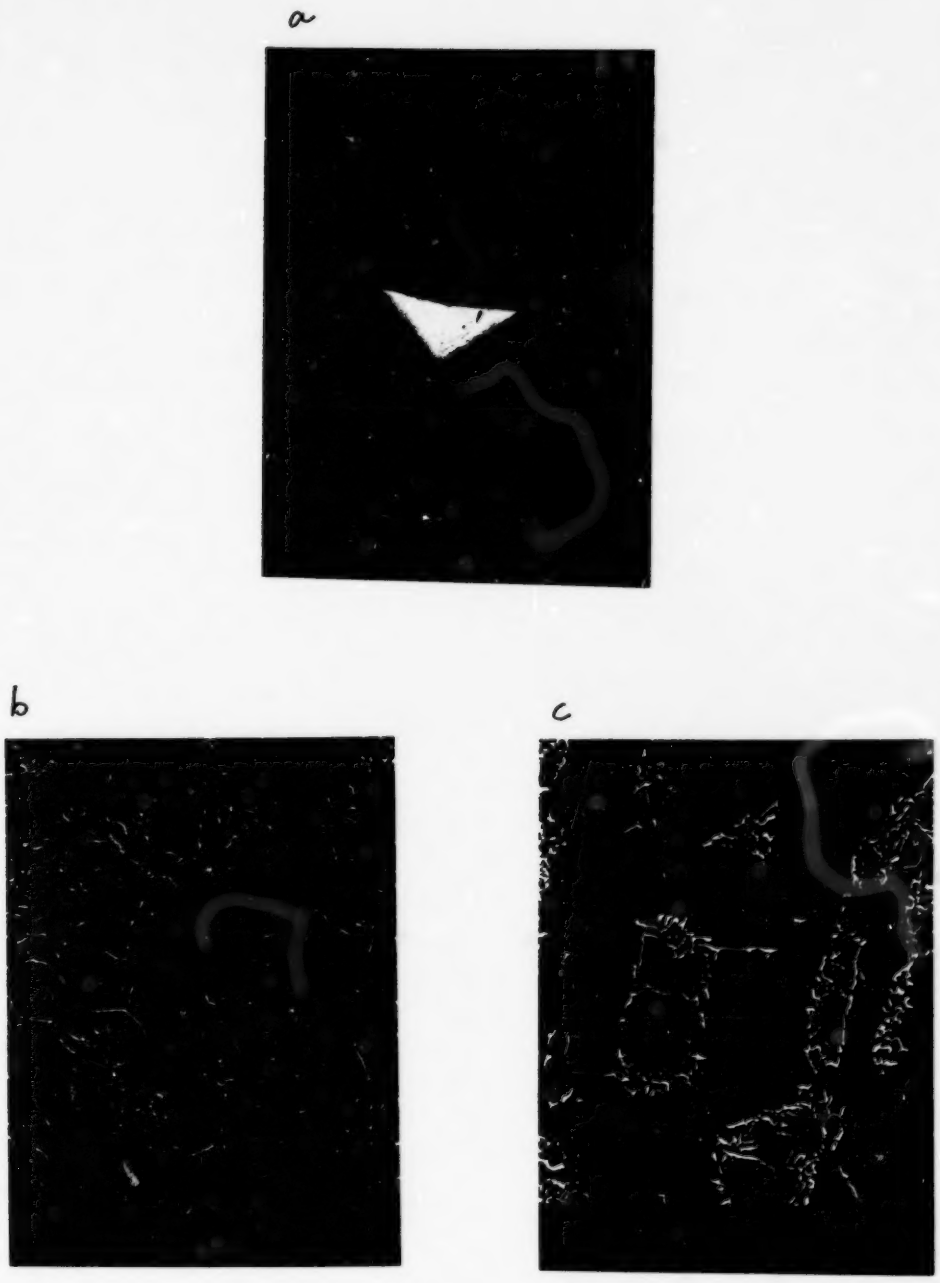

Fig. 7 Intercritical region of sample K31 (a) At low magnification both the intercritical (left) and subcritical (right) areas are visible (x120); The microstructures of these two regions are shown at higher magnification in (b) and (c) (x1000)

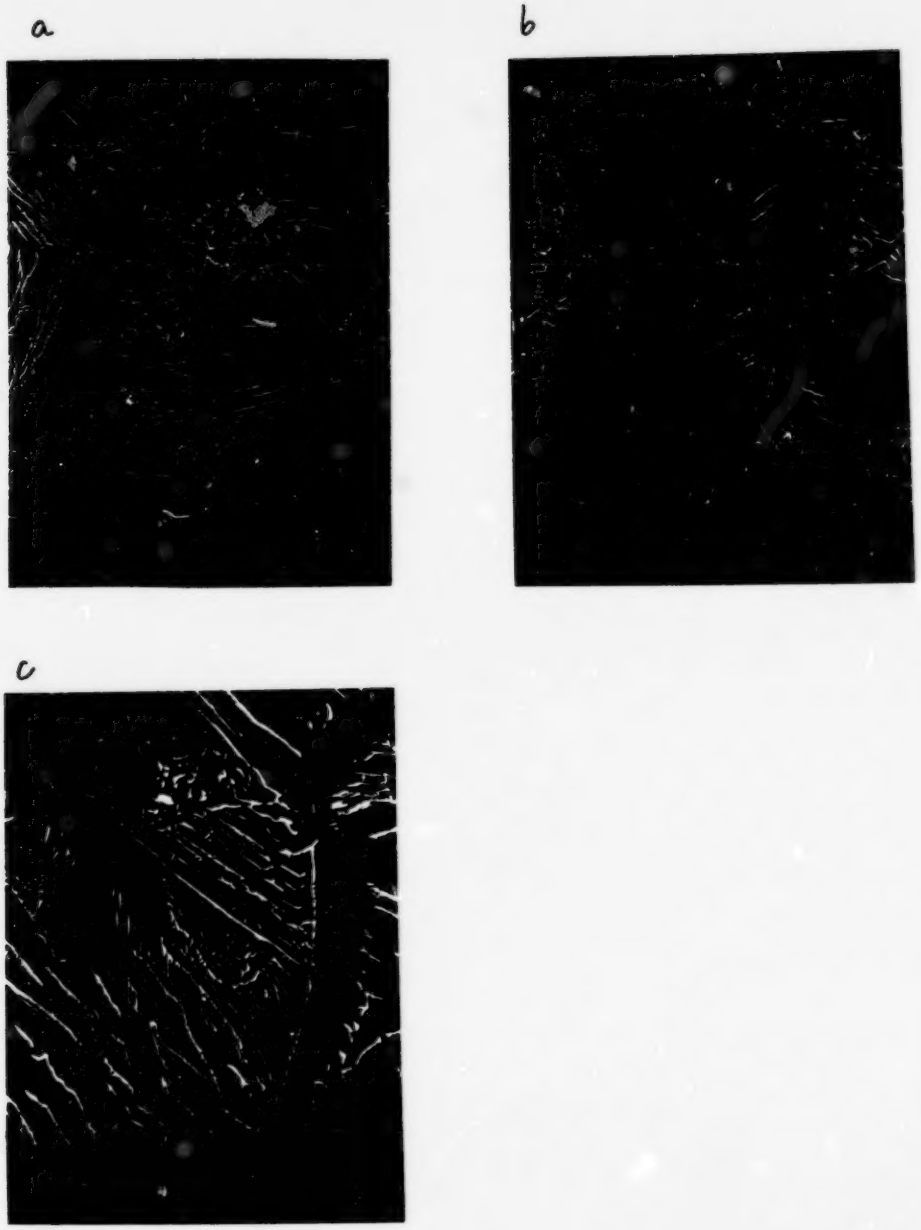

Fig. 8 Sample K31, coarse-grained heat affected zone region (a) SEM, low magnification showing proeutectoid ferrite, Widmanstatten ferrite and fine pearlite (x300); as (b) (x1000); (c) sample K72, C.G.H.A.Z. structure, similar to K31 but the proporiton of ferrite is greater (x1000)

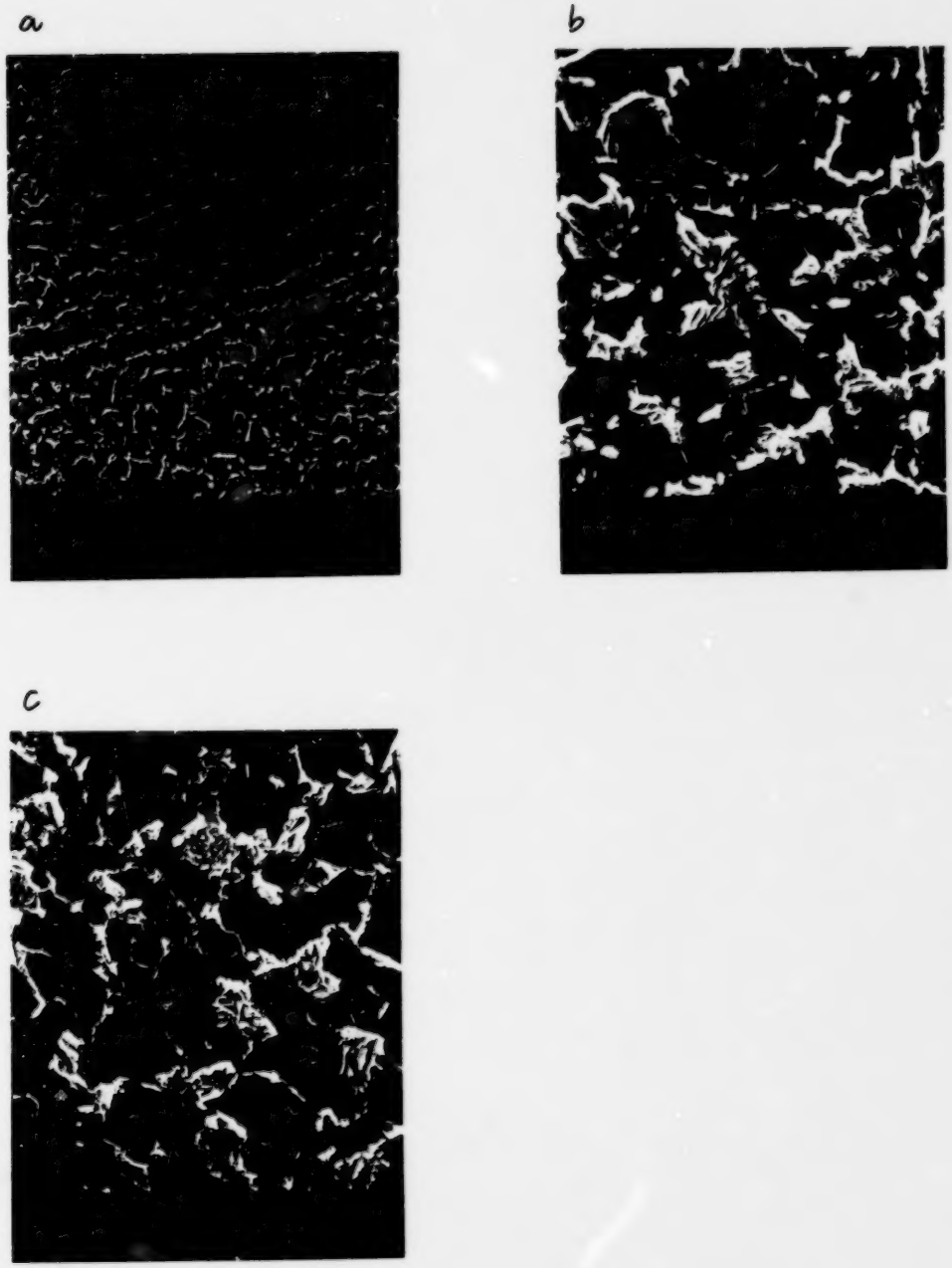

Fig. 9 (a) Microstructure of base plate B showing a ferrite-pearlite microstructure (x300); (b) as (a) (x1000); (c) sub-critical region of HAZ of sample B31 (x1000)

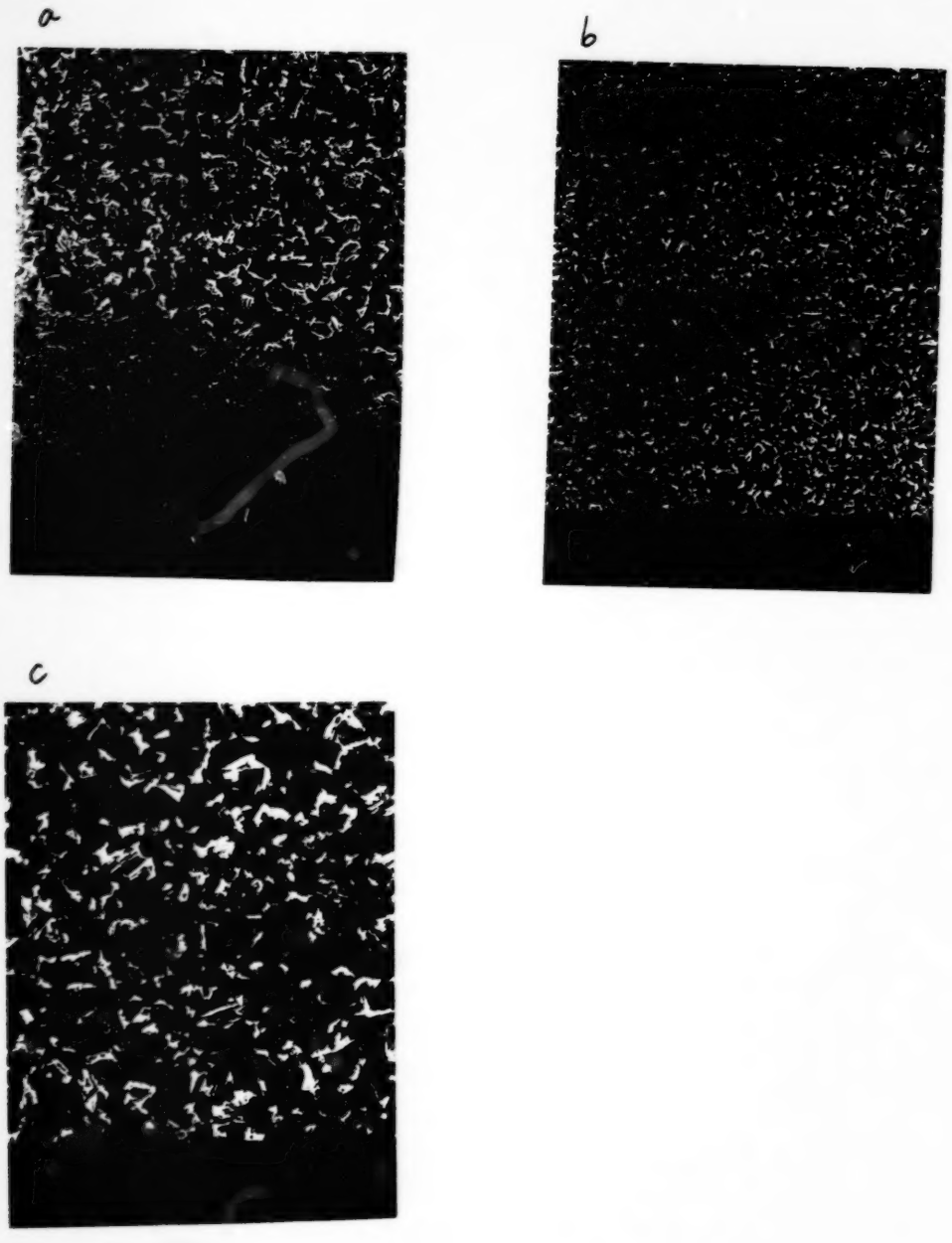

Fig. 10 (a) Intercritical-sub-critical region of steel B (x300); (b) as (a), same magnification but totally within the intercritical region (x300); (c) break-up of pearlite and formation of bainitic structure can be seen at higher magnfication (x1000)

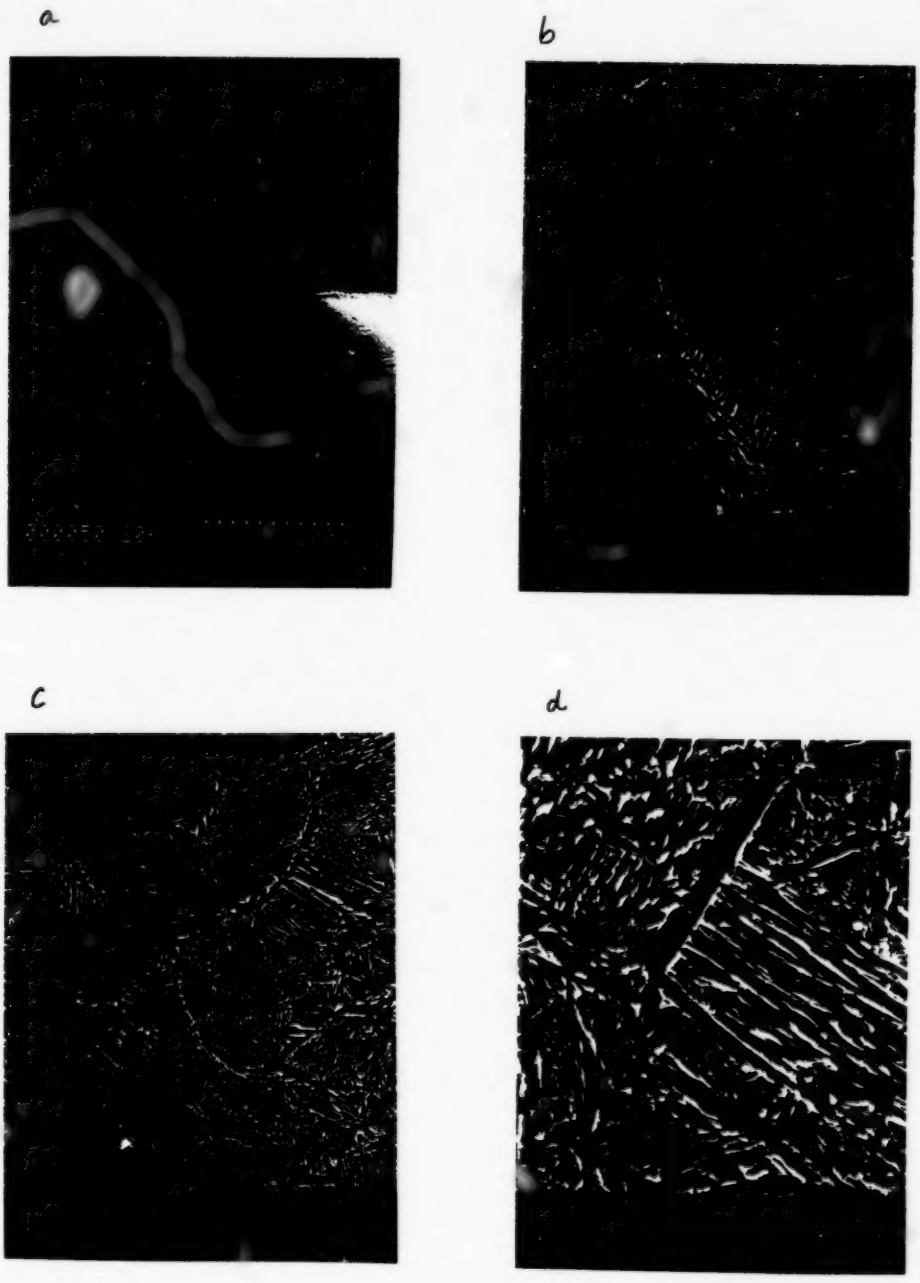

Fig. 11 Sample B31, coarse-grained heat affected zone region (a) SEM, low magnification, no proeutectoid ferrite is visible (cf samples K31 and F31) x300; (b) as (a) showing lower bainite structure (x1000). Sample B72, coarse grained heat affected zone region; (c) SEM, low magnification showing proeutectoid ferrite and upper bainite (x300); (d) as (c) (x1000)